A Review of Curvelets and Recent Applications

Jianwei Ma[1,2] and Gerlind Plonka[3]

[1] School of Aerospace, Tsinghua University, Beijing 100084, China
[2] Centre de Geosciences, Ecole des Mines de Paris, 77305 Fontainebleau Cedex, France
[3] Department of Mathematics, University of Duisburg-Essen, 47048 Duisburg, Germany

Abstract

Multiresolution methods are deeply related to image processing, biological and computer vision, scientific computing, etc. The curvelet transform is a multiscale directional transform, which allows an almost optimal nonadaptive sparse representation of objects with edges. It has generated increasing interest in the community of applied mathematics and signal processing over the past years. In this paper, we present a review on the curvelet transform, including its history beginning from wavelets, its logical relationship to other multiresolution multidirectional methods like contourlets and shearlets, its basic theory and discrete algorithm. Further, we consider recent applications in image/video processing, seismic exploration, fluid mechanics, simulation of partial different equations, and compressed sensing.

Keywords: curvelets, wavelets, multiscale geometric analysis, image processing, biological and computer vision, seismic exploration, turbulence, surface metrology, compressed sensing

1 Introduction

Digital images are two-dimensional matrices in image processing. One important task is to adjust the values of these matrices in order to get clear features in images. The adjusting of values obeys a certain mathematical model. The main challenge is how to build suitable mathematical models for practical requirements. Taking image denoising as an example, many mathematical models are based on a frequency partition of the image, where components with high frequency are interpreted as noise that have to be removed while those with low frequency are seen as features to be remained. Curvelets, which are going to be reviewed in this paper, can be seen as an effective model that not only considers a multiscale time-frequency local partition but also makes use of the direction of features.

Most natural images/signals exhibit line-like edges, i.e., discontinuities across curves (so-called line or curve singularities). Although applications of wavelets have become increasingly popular in scientific and engineering fields, traditional wavelets perform well only at representing point singularities, since they ignore the geometric properties of structures and do not exploit the regularity of edges. Therefore, wavelet-based compression, denoising, or structure extraction become computationally inefficient for geometric features with line and surface singularities. For example, when we download compressed images or videos, we often find a mosaic phenomenon (i.e., block artifacts along edges of the images). This mosaic phenomenon mainly results from the poor ability of wavelets to handle line singularities. In fluid mechanics, discrete wavelet thresholding often leads to oscillations along edges of the coherent eddies, and consequently, to the deterioration of the vortex tube structures, which in turn can cause an unphysical leak of energy into neighboring scales producing an artificial "cascade" of energy.

Multiscale methods are also deeply related with biological and computer vision. Since, Olshausen and Field's work in Nature (1996) [62], researchers in biological vision have re-iterated the similarity between vision and multiscale image processing. It has been recognized that the receptive fields of simple cells in a mammalian primary visual cortex can be characterized as being spatially localized, oriented and bandpass (selective to structure at different spatial scales). Therefore, they can be well represented by wavelet transforms. One approach to understand the response properties of visual neurons has been to consider their relationship to the statistical structure of natural images in terms of efficient coding. A coding strategy that maximizes sparseness is sufficient to account for the similar properties of simple-cell receptive fields [62, 63]. The wavelet transform yields sparse image representations, and hence provides an efficient way to understand the localized, oriented, bandpass receptive files, similar to those found in the primary visual cortex. However, wavelets do not supply a good direction selectivity, which is also an important response property of simple cells and neurons at stages of the visual pathway. Therefore, a directional multiscale sparse coding is desirable in this field.

One of the primary tasks in computer vision is to extract features from an image or a sequence of images [57]. The features can be points, lines, edges, and textures. A given feature is characterized by position, direction, scale and other property parameters. The most common technique, used in early vision for extraction of such features, is linear filtering, which is also reflected in models used in biological visual systems, i.e., human visual motion sensing. Objects at different scales can arise from distinct physical processes. This leads to the use of scale space filtering and multiresolution wavelet transform in this field. An important motivation for computer vision is to obtain directional representations which capture anisotropic lines and edges while providing sparse decompositions.

A multiresolution geometric analysis (MGA), named curvelet transform, was proposed [8, 10, 11, 12, 13] in order to overcome the drawbacks of conventional two-dimensional discrete wavelet transforms. In the two-dimensional (2D) case, the curvelet transform allows an almost optimal sparse representation of objects with C^2-singularities. For a smooth object f with discontinuities along C^2-continuous curves, the best m-term approximation $\tilde{f}_m$ by curvelet thresholding obeys $\|f - \tilde{f}_m\|_2^2 \leq Cm^{-2} (\log m)^3$, while for wavelets the decay rate is only m^{-1}. Combined with other methods, excellent performance of the curvelet transform has been shown in image processing, see e.g. [47, 55, 50, 69, 70]. Unlike the isotropic elements of wavelets, the needle-shaped elements of this transform possess very high directional sensitivity and anisotropy (see Fig. 1 for the $2D$ case). Such elements are very efficient in representing line-like edges. Recently, the curvelet transform has been extended to three dimensions by Ying et al. [8, 77].

Let us roughly compare the curvelet system with the conventional Fourier and wavelet analysis. The short-time Fourier transform uses a shape-fixed rectangle in Fourier domain, and conventional wavelets use shape-changing (dilated) but area-fixed windows. By contrast, the curvelet transform uses angled polar wedges or angled trapezoid windows in frequency domain in order to resolve also directional features.

The theoretic concept of curvelets is easy to understand, but how to achieve the discrete algorithms for practical applications is challenging. In the following, we first address a brief history of curvelets starting from classical wavelets. We also mention some other wavelet constructions that aim to improve the representation of oriented features towards visual reception and image processing. Then we will have a closer look at the definition and the properties of the continuous curvelet transform. We derive the discrete curvelet frame and the corresponding fast algorithm for the discrete curvelet transform in the two- and three-dimensional case. In
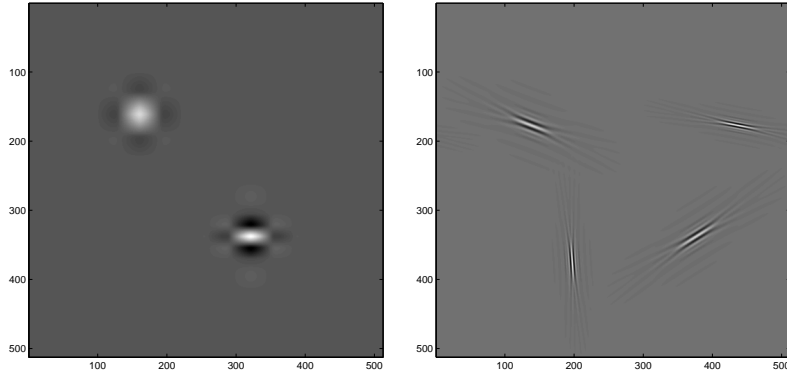
Figure 1: The elements of wavelets (left) and curvelets on various scales, directions and translations in the spatial domain (right). Note that the tensor-product 2D wavelets are not strictly isotropic but have directional selectivity.

particular, we present the construction of a curvelet system and its discretization by means of a typical example of "second generation curvelets". Finally, we show some recent applications of the curvelet transform in image and seismic processing, fluid mechanics, numerical treatment of partial differential equations, and compressed sensing.

2   FROM CLASSICAL WAVELETS TO CURVELETS

As outlined in the introduction, although the discrete wavelet transform (DWT) has established an impressive reputation as a tool for mathematical analysis and signal processing, it has the disadvantage of poor directionality, which has undermined its usage in many applications. Significant progress in the development of directional wavelets has been made in recent years. The complex wavelet transform is one way to improve directional selectivity and only requires $\mathcal{O}(N)$ computational cost. However, the complex wavelet transform has not been widely used in the past, since it is difficult to design complex wavelets with perfect reconstruction properties and good filter characteristics [33, 60]. One popular technique is the dual-tree complex wavelet transform (DT CWT) proposed by Kingsbury [41, 42], which added perfect reconstruction to the other attractive properties of complex wavelets, including approximate shift invariance, six directional selectivities, limited redundancy and efficient $\mathcal{O}(N)$ computation.

The 2D complex wavelets are essentially constructed by using tensor-product 1D wavelets. The directional selectivity provided by complex wavelets (six directions) is much better than that obtained by the classical DWT (three directions), but is still limited.

In 1999, an anisotropic geometric wavelet transform, named ridgelet transform, was proposed by Candès and Donoho [5, 9]. The ridgelet transform is optimal at representing straight-line singularities. This transform with arbitrary directional selectivity provides a key to the analysis of higher dimensional singularities. Unfortunately, the ridgelet transform is only applicable to objects with global straight-line singularities, which are rarely observed in real applications [52]. In order to analyze local line or curve singularities, a natural idea is to consider a partition for the image, and then to apply the ridgelet transform to the obtained sub-images. This block ridgelet based transform, which is named curvelet transform, was first proposed by Candès and Donoho in 2000, see [10]. Apart from the blocking effects, however, the application of this so-called

first-generation curvelet transform is limited because the geometry of ridgelets is itself unclear, as they are not true ridge functions in digital images. Later, a considerably simpler second-generation curvelet transform based on a frequency partition technique was proposed by the same authors, see [11, 12, 13]. Recently, a variant of the second-generation curvelet transform was proposed to handle image boundaries by mirror extension (ME) [22]. Previous versions of the transform treated image boundaries by periodization. Here, the main modifications are to tile the discrete cosine domain instead of the discrete Fourier domain, and to adequately reorganize the data. The obtained algorithm has the same computational complexity as the standard curvelet transform.

The second-generation curvelet transform [11, 12, 13] has been shown to be a very efficient tool for many different applications in image processing, seismic data exploration, fluid mechanics, and solving PDEs (partial different equations). In this survey, we will focus on this successful approach, and show its theoretical and numerical aspects as well as the different applications of curvelets. From the mathematical point of view, the strength of the curvelet approach is their ability to formulate strong theorems in approximation and operator theory. The discrete curvelet transform is very efficient in representing curve-like edges. But the current curvelet systems still have two main drawbacks: 1) they are not optimal for sparse approximation of curve features beyond C^2-singularities; 2) the discrete curvelet transform is highly redundant. The currently available implementations of the discrete curvelet transform (see www.curvelet.org) aim to reduce the redundancy smartly. However, independently from the good theoretical results on N-term approximation by curvelets, the discrete curvelet transform is not appropriate for image compression. The question of how to construct an orthogonal curvelet-like transform is still open.

3   Relationship of curvelets to other directional wavelets

There have been several other developments of directional wavelet systems in recent years with the same goal, namely a better analysis and an optimal representation of directional features of signals in higher dimensions. Non of these approaches has reached the same publicity as the curvelet transform. However, we want to mention shortly some of these developments and also describe their relationship to curvelets.

Steerable wavelets [32, 67], Gabor wavelets [44], wedgelets [26], beamlets [27], bandlets [58, 61], contourlets [24], shearlets [43, 35], wave atoms [23], platelets [76], surfacelets [46], have been proposed independently to identify and restore geometric features. These geometric wavelets or directional wavelets are uniformly called X-lets.

The steerable wavelets [32, 67] and Gabor wavelets [44] can be seen as early directional wavelets. The steerable wavelets were built based on directional derivative operators (i.e., the second derivative of a Gaussian), while the Gabor wavelets were produced by a Gabor kernel that is a product of an elliptical Gaussian and a complex plane wave. In comparison to separable orthonormal wavelets, the steerable wavelets provide translation-invariant and rotation-invariant representations of the position and the orientation of considered image structures. Applications of Gabor wavelets focused on image classification and texture analysis. Gabor wavelets have also been used for modeling the receptive field profiles of cortical simple cells. Applications of Gabor wavelets suggested that the precision in resolution achieved through redundancy may be a more relevant issue in brain modeling, and that orientation plays a key role in the primary

visual cortex. The main differences between steerable wavelets/Gabor wavelets and other X-lets is that the early methods do not allow for a different number of directions at each scale while achieving nearly critical sampling.

Contourlets, as proposed by Do and Vetterli [24], form a discrete filter bank structure that can deal effectively with piecewise smooth images with smooth contours. This discrete transform can be connected to curvelet-like structures in the continuous domain. Hence, the contourlet transform [24] can be seen as a discrete form of a particular curvelet transform. Curvelet constructions require a rotation operation and correspond to a partition of the 2D frequency plane based on polar coordinates. This property makes the curvelet idea simple in the continuous domain but causes problems in the implementation for discrete images. In particular, approaching critical sampling seems difficult in discretized constructions of curvelets. For contourlets, it is easy to implement the critically sampling. There exists an orthogonal version of contourlet transform that is faster than current discrete curvelet algorithms [8]. The directional filter bank, as a key component of contourlets, has a convenient tree-structure, where aliasing is allowed to exist and will be canceled by carefully designed filters. Thus, the key difference between contourlets and curvelets is that the contourlet transform is directly defined on digital-friendly discrete rectangular grids. Unfortunately, contourlet functions have less clear directional geometry/features than curvelets (i.e., more oscillations along the needle-like elements) leading to artifacts in denoising and compression.

Surfacelets [46] are 3D extensions of the 2D contourlets that are obtained by a higher-dimensional directional filter bank and a multiscale pyramid. They can be used to efficiently capture and represent surface-like singularities in multidimensional volumetric data involving biomedical imaging, seismic imaging, video processing and computer vision. Surfacelets and the 3D curvelets that will be addressed in Section 6 aim at the same frequency partitioning, but the two transforms achieve this goal with two very different approaches as we described above in the 2D case. The surfacelet transform is less redundant than the 3D curvelet transform, and this advantage is payed by a certain loss of directional features.

Unlike curvelets, the shearlets [43, 35] form an affine system with a single generating mother shearlet function parameterized by a scaling, a shear, and a translation parameter, where the shear parameter captures the direction of singularities. It has been shown that both the curvelet and shearlet transforms have the same decay rates [13, 35]. Indeed, using the fast curvelet transform based on transition to Cartesian arrays, described in Section 5.2, the discrete implementations of the two transforms are very similar [8, 29].

The bandlet transform [58, 61] is based on adaptive techniques and has a good performance for images with textures beyond C^2-singularities, but it has to pay much higher computational cost for its adaptation.

In this paper we are not able to give a more detailed overview on all these approaches and refer to the given references for further information.

4 THE CONTINUOUS CURVELET TRANSFORM (CCT) IN $\mathbb{R}^2$

In this section we describe the CCT developed in [11, 12]. We present the construction of a second generation curvelet system. In particular, we illustrate the necessary steps to achieve a complete curvelet frame.

We work in $\mathbb{R}^2$ and we denote with $x = (x_1, x_2)^T$ the spatial variable, and with $\xi = (\xi_1, \xi_2)^T$

the variable in frequency domain. Further, let $r = \sqrt{\xi_1^2 + \xi_2^2}$, $\omega = \arctan \frac{\xi_1}{\xi_2}$ be the polar coordinates in frequency domain.

How can the elements of the continuous curvelet transform be constructed? What properties do they have in time and in frequency domain? Why is the continuous curvelet transform of interest? Let us consider these questions more closely.

4.1 Window functions

For constructing the curvelet functions we first need to define special window functions that satisfy certain admissibility conditions. We present an explicit example that is representative for all possible choices of window functions being the fundament of the curvelet construction. For this purpose, let us consider the scaled Meyer windows (see [21], p. 137)

$$V(t) = \begin{cases} 1 & |t| \leq 1/3, \\ \cos[\frac{\pi}{2}\nu(3|t| - 1)] & 1/3 \leq |t| \leq 2/3, \\ 0 & \text{else,} \end{cases}$$

$$W(r) = \begin{cases} \cos[\frac{\pi}{2}\nu(5 - 6r)] & 2/3 \leq r \leq 5/6, \\ 1 & 5/6 \leq r \leq 4/3, \\ \cos[\frac{\pi}{2}\nu(3r - 4)] & 4/3 \leq r \leq 5/3, \\ 0 & \text{else,} \end{cases}$$

where ν is a smooth function satisfying

$$\nu(x) = \begin{cases} 0 & x \leq 0, \\ 1 & x \geq 1, \end{cases} \qquad \nu(x) + \nu(1 - x) = 1, \quad x \in \mathbb{R}.$$

For the simple case $\nu(x) = x$ in $[0, 1]$, the window functions $V(t)$ and $W(r)$ are plotted in Figure 2. In order to obtain smoother functions W and V, we need to take smoother functions ν. We may use the polynomials $\nu(x) = 3x^2 - 2x^3$ or $\nu(x) = 5x^3 - 5x^4 + x^5$ in $[0, 1]$, such that ν is in $C^1(\mathbb{R})$ or in $C^2(\mathbb{R})$. As we will see later, the curvelet elements will be obtained as the inverse Fourier transform of a suitable product of the above windows. Therefore, the smoothness of V and W will ensure a faster decay of the curvelet elements in time domain. An example of an arbitrarily smooth window ν is given by

$$\nu(x) = \begin{cases} 0 & x \leq 0, \\ \frac{s(x-1)}{s(x-1)+s(x)} & 0 < x < 1, \\ 1 & x \geq 1, \end{cases} \qquad \text{with} \quad s(x) = e^{-\left(\frac{1}{(1+x)^2} + \frac{1}{(1-x)^2}\right)}.$$

The above two functions $V(t)$ and $W(r)$ satisfy the conditions

$$\sum_{l=-\infty}^{\infty} V^2(t - l) = 1, \quad t \in \mathbb{R}, \tag{1}$$

$$\sum_{j=-\infty}^{\infty} W^2(2^j r) = 1, \quad r > 0. \tag{2}$$

For $V(t)$, this can be simply observed. Since supp $V \subset [-1, 1]$, for a fixed $t \in \mathbb{R}$ the above sum has only two nonvanishing terms, and for $t \in [1/3, 2/3]$ we find with the substitution
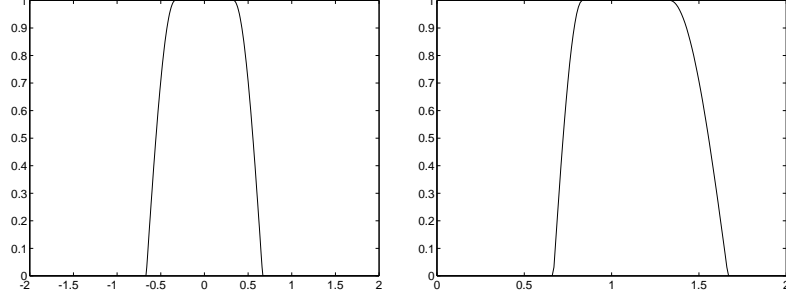
6

Figure 2: Plot of the windows $V(t)$ (left) and $W(r)$ (right).

$s = 3t - 1$

$$\sum_{l=-\infty}^{\infty} V^2(t-l) = V^2(t) + V^2(t-1) = \cos^2[\frac{\pi}{2}\nu(3t-1)] + \cos^2[\frac{\pi}{2}\nu(3|t-1|-1)]$$

$$= \cos^2[\frac{\pi}{2}\nu(s)] + \cos^2[\frac{\pi}{2}\nu(1-s)] = \cos^2[\frac{\pi}{2}\nu(s)] + \cos^2[\frac{\pi}{2}(1-\nu(s))]$$

$$= \cos^2[\frac{\pi}{2}\nu(s)] + \sin^2[\frac{\pi}{2}\nu(s)] = 1.$$

Similarly, formula (2) can be shown for W. We have supp $W(2^j \cdot) \subset [2^{-j-1}, 2^{-j+1}]$, and for a fixed $r \in [1/2, 1]$, it follows that $\sum_{j=-\infty}^{\infty} W^2(2^{-j}r) = W^2(r) + W^2(2r)$. Applying the definition of W we find in the interval $[1/2, 1]$

$$W^2(r) + W^2(2r) = \begin{cases} 1 & 1/2 \le r \le 2/3, \\ \cos^2[\frac{\pi}{2}(\nu(6r-4)] + \cos^2[\frac{\pi}{2}(\nu(5-6r)] & 2/3 \le r \le 5/6, \\ 1 & 5/6 \le r \le 1, \end{cases}$$

where we can show $\cos^2[\frac{\pi}{2}(\nu(6r-4)] + \cos^2[\frac{\pi}{2}(\nu(5-6r)] = 1$, similarly as before. Moreover, the above two windows also satisfy the normalization conditions

$$\int_0^\infty W^2(r) \frac{dr}{r} = \ln 2, \tag{3}$$

$$\int_{-1}^1 V^2(t) \, dt = 1. \tag{4}$$

Indeed, we observe that

$$1 = \sum_{l=-\infty}^{\infty} V^2(t-l) = \int_0^1 \sum_{l=-\infty}^{\infty} V^2(t-l) \, dt = \int_{-\infty}^\infty V^2(t) \, dt$$

and substituting $r \in (0, \infty)$ by 2^t with $t \in (-\infty, \infty)$ we find

$$1 = \sum_{j=-\infty}^{\infty} W^2(2^j r) = \sum_{j=-\infty}^{\infty} W^2(2^{j+t}) = \int_0^1 \sum_{j=-\infty}^{\infty} W^2(2^{j+t}) \, dt$$

$$= \sum_{j=-\infty}^{\infty} \frac{1}{\ln 2} \int_{2^j}^{2^{j+1}} W^2(s) \frac{ds}{s} = \frac{1}{\ln 2} \int_0^\infty W^2(s) \frac{ds}{s},$$
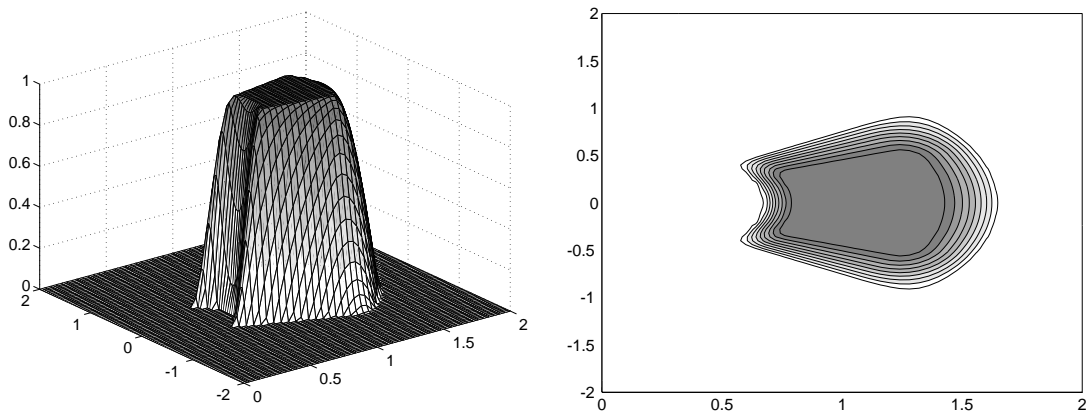
7

Figure 3: Window $U_1(\xi)$ (left) and its support (right).

Hence, the window functions V and W satisfy the conditions (3) and (4) that are called *admissibility conditions* for V and W for the continuous curvelet transform. Analogously, the conditions (1) and (2) are necessary admissibility conditions for the discrete curvelet transform.

4.2   System of curvelet functions

Assume now that the two window functions $V(t)$ and $W(r)$ satisfy the admissibility conditions (1)-(4). These windows will be used to construct a family of complex-valued waveforms with three parameters,

the *scale* $a \in (0, 1]$,

the *location* $b \in \mathbb{R}^2$,

and the *orientation* $\theta \in [0, 2\pi)$.

Let the Fourier transform for a function $f \in L^2(\mathbb{R}^2)$ be defined by

$$\widehat{f}(\xi) := \frac{1}{2\pi} \int_{\mathbb{R}^2} f(x)\, e^{-i\langle x, \xi \rangle}\, dx.$$

Using the polar coordinates (r, ω) in frequency domain, we now define the a-scaled window

$$U_a(r, w) := a^{3/4} W(ar)\, V\left(\frac{\omega}{\sqrt{a}}\right)$$

for some a with $0 < a \leq 1$. The support of U_a is a polar wedge depending on the supports of W and V, see Figure 3 for $a = 1$, and Figure 4 for $a = 1/2$ and $a = 1/8$. Comparing these supports in Figure 4, we nicely see the effect of scaling. While supp $W(a\cdot) \subset [1/2a, 2/a]$ is growing for decreasing $a \in (0, 1]$, the support $[-2\sqrt{a}/3, 2\sqrt{a}/3]$ of $V(\cdot/\sqrt{a})$ gets smaller, such that the wedges U_a become longer and thinner for decreasing a.

The window U_a is now applied for building curvelet functions as follows. Let $\varphi_{a,0,0} \in L^2(\mathbb{R}^2)$ be given by its Fourier transform

$$\widehat{\varphi}_{a,0,0}(\xi) := U_a(\xi),$$

8

and let the curvelet family be generated by translation and rotation of the basic element $\varphi_{a,0,0}$,

$$\varphi_{a,b,\theta}(x) := \varphi_{a,0,0}(R_\theta(x-b)), \tag{5}$$

with the translation $b \in \mathbb{R}^2$, and where $R_\theta = \begin{pmatrix} \cos\theta & -\sin\theta \\ \sin\theta & \cos\theta \end{pmatrix}$ is the 2×2 rotation matrix with angle θ.

Observe that the rotation in spatial domain with an angle θ corresponds to a rotation in frequency domain with θ since

$$\widehat{\varphi}_{a,b,\theta}(\xi) = e^{-i\langle b, \xi \rangle} \widehat{\varphi}_{a,0,0}(R_\theta \xi) = e^{-i\langle b, \xi \rangle} U_a(R_\theta \xi).$$

Let us have a closer look at the properties of the functions $\varphi_{a,b,\theta}$.

Support in frequency domain

From the above equation we observe $\operatorname{supp} \widehat{\varphi}_{a,b,\theta} = \operatorname{supp} U_a(R_\theta \xi)$. In particular, the support of $\widehat{\varphi}_{a,b,\theta}$ does not at all depend on the translation parameter b. For $\theta = 0$, $\operatorname{supp} \widehat{\varphi}_{a,b,0}$ can be seen in Figures 3 and 4 for different a. For $\theta \in [0, 2\pi)$, this support is rotated by θ (clockwise). The curvelet functions $\varphi_{a,b,\theta}$ are complex functions. One is able to construct a real counterpart by replacing the function $W(ar)$ in the window $U_a(r, w)$ by $W(r) + W(-r)$; in this case $\widehat{\varphi}_{a,b,\theta}$ is supported on two polar wedges being symmetric with respect to zero.
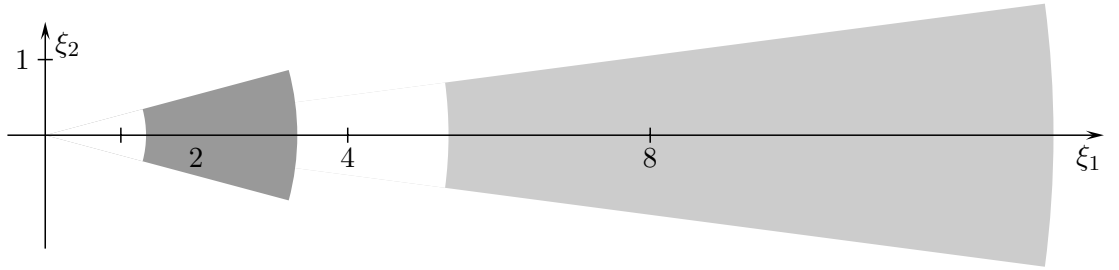

Figure 4: Supports of the windows $U_{1/2}(\xi)$ (grey) $U_{1/8}(\xi)$ (light grey).

Support in time domain and oscillation properties

In time domain, things are more involved. Since $\widehat{\varphi}_{a,b,\theta}$ has compact support, the curvelet function $\varphi_{a,b,\theta}$ cannot have compact support in time domain. From Fourier analysis, one knows that the decay of $\varphi_{a,b,\theta}(x)$ for large $|x|$ depends on the smoothness of $\widehat{\varphi}_{a,b,\theta}$ in frequency domain. The smoother $\widehat{\varphi}_{a,b,\theta}$, the faster the decay.

By definition, $\widehat{\varphi}_{a,0,0}$ is supported away from the vertical axis $\xi_1 = 0$ but near the horizontal axis $\xi_2 = 0$, see Figure 4. Hence, for small $a \in (0, 1]$ the function $\varphi_{a,0,0}$ is less oscillatory in x_2-direction (with frequency about $\sqrt{a}$) and very oscillatory in x_1-direction (containing frequencies of about $1/2a$). The *essential support* of the amplitude spectrum of $\varphi_{a,0,0}$ is a rectangle of size $[-\pi/2a, \pi/2a] \times [-\pi/\sqrt{a}, \pi/\sqrt{a}]$, and the decay of $\varphi_{a,0,0}$ away from this rectangle essentially depends on the smoothness of U_a resp. the function ν used in the windows V and W. Now, from (5) we simply observe that the essential support of $\varphi_{a,b,\theta}$ is the rectangle rotated by the angle θ and translated by $R_\theta b$.

9

Vanishing moments

Observe that $\varphi_{a,b,\theta}$ are C^∞ complex functions. Since the compact support of $\widehat{\varphi}_{a,b,\theta}$ is away from $(0,0)$, the functions $\varphi_{a,b,\theta}$ have mean value zero. Moreover, $\widehat{\varphi}_{a,b,\theta}$ has infinitely many directional moments, i.e., for all bivariate polynomials $p(x)$ with $x \in \mathbb{R}^2$ of arbitrary degree and for all angles $\tilde{\theta}$ we find

$$\int_{\mathbb{R}^2} p(R_{\tilde{\theta}} x)\, \varphi_{a,b,\theta}(x)\, dx = 0,$$

where again $R_{\tilde{\theta}}$ denotes the rotation matrix with the angle $\tilde{\theta}$. This observation is a direct consequence of the smoothness of $\varphi_{a,b,\theta}$, see e.g. [21], page 153, for the univariate case.

4.3 Definition of the continuous curvelet transform

Applying the family of high frequency elements

$$\{\varphi_{a,b,\theta} : a \in (0,1],\, b \in \mathbb{R}^2,\, \theta \in [0, 2\pi)\}, \tag{6}$$

the *continuous curvelet transform* Γ_f of $f \in L^2(\mathbb{R}^2)$ is given as

$$\Gamma_f(a, b, \theta) := \langle \varphi_{a,b,\theta},\, f \rangle = \int_{\mathbb{R}^2} \varphi_{a,b,\theta}(x)\, \overline{f(x)}\, dx,$$

i.e., one needs to compute the L^2 scalar products of a given function f with each curvelet element $\varphi_{a,b,\theta}$. Observe that we have bounded the scale a from above by $a = 1$, that means, low frequency functions are not contained in the system (6).

For functions $f \in L^2(\mathbb{R}^2)$ possessing a Fourier transform that vanishes for $|\xi| < 2$, the curvelet coefficients $\langle \varphi_{a,b,\theta},\, f \rangle$ contain the complete information about f, i.e., the continuous curvelet transform is invertible for these functions f, and there exists a reproducing formula to compute f from $\langle \varphi_{a,b,\theta},\, f \rangle$, $a \in (0,1], b \in \mathbb{R}^2$, $\theta \in [0, 2\pi)$, see [12]. One can extend the transform to low frequencies as follows. We consider

$$\widehat{\Psi}^2(\xi) := \frac{1}{\ln 2} \int_0^{|\xi|} |W(r)|^2\, \frac{dr}{r}.$$

By supp $W = [2/3, 5/3]$ and $\int_0^\infty W^2(r)/r\, dr = \ln 2$, we obviously have $\widehat{\Psi}^2(\xi) = 1$ for $|\xi| \geq 5/3$ and $\widehat{\Psi}^2(\xi) = 0$ for $|\xi| < 2/3$. Let now the function $\Phi \in L^2(\mathbb{R}^2)$ be given by its Fourier transform

$$\widehat{\Phi}(\xi) := \begin{cases} 1 & |\xi| \leq 1/2, \\ (1 - \widehat{\Psi}^2(\xi))^{1/2} & 1/2 < |\xi| < 2, \\ 0 & |\xi| \geq 2, \end{cases}$$

and let $\Phi_b(x) := \Phi(x - b)$, $b \in \mathbb{R}^2$ be the *father wavelets*.

Indeed, one can show that for all $f \in L^2(\mathbb{R}^2)$ it follows now the reproducing formula

$$f(x) = \int_{\mathbb{R}^2} \langle \Phi_b, f \rangle \Phi_b(x)\, db + \frac{1}{(\ln 2)} \int_0^{2\pi} \int_{\mathbb{R}^2} \int_0^1 \langle \varphi_{a,b,\theta}, f \rangle \varphi_{a,b,\theta}(x)\, \frac{da}{a^{3/2}}\, \frac{db}{a^{1/2}}\, \frac{d\xi}{a},$$

i.e., the CCT is now invertible for all $\langle \varphi_{a,b,\theta},\, f \rangle$, see [12].

10

Since the CCT involves an infinite number of curvelet coefficients $\langle \varphi_{a,b,\theta}, f \rangle$ (with the cardinal number of the continuum), it is not directly suitable for practical purposes. It has been successively applied to analyze different singularities of two-dimensional functions along lines and along smooth curves, see [11, 13]. For further applications we refer to Section 7. The CCT is closely related to the continuous transforms used by Hart Smith [68], and to the FBI and the Wave Packets transform, see [4, 11, 20].

5 THE FAST CURVELET TRANSFORM

For numerical computations we need to discretize the continuous curvelet transform, since we usually work with discrete data sets in applications. As shown in [12], a discrete version of the continuous curvelet transform can be derived by a suitable sampling at the range of scales, orientations and locations.

5.1 The discrete curvelet transform

We choose

- the scales $a_j := 2^{-j}$, $j \geq 0$;

- the equidistant sequence of rotation angles $\theta_{j,l}$,

$$\theta_{j,l} := \frac{\pi l \, 2^{-\lceil j/2 \rceil}}{2} \qquad \text{with} \quad l = 0, 1, \ldots, 4 \cdot 2^{\lceil j/2 \rceil} - 1;$$

(Here $\lceil x \rceil$ denotes the smallest integer being greater than or equal to x.)

- the positions $b_k^{j,l} = b_{k_1,k_2}^{j,l} := R_{\theta_{j,l}}^{-1} (\frac{k_1}{2^j}, \frac{k_2}{2^{j/2}})^T$, with $k_1, k_2 \in \mathbb{Z}$, and where R_θ denotes the rotation matrix with angle θ.

This choice will lead to a discrete curvelet system that forms a tight frame, i.e., every function $f \in L^2(\mathbb{R})$ will be representable by a curvelet series, and hence the discrete curvelet transform will be invertible.

For example, for $j = 0$ we consider the angles $\theta_{0,l} = \pi l/2$, $l = 0, 1, 2, 3$ and the positions $\{b_k^{0,l}\}_{k \in \mathbb{Z}, l=0,1,2,3} = \mathbb{Z}^2$. For $j = 4$, the angles $\theta_{4,l} = \pi l/8$, $l = 0, \ldots, 15$ occur, and, depending on the angles $\theta_{4,l}$, eight different grids for translation are considered, where rectangles of size $1/16 \times 1/4$ are rotated by $\theta_{4,l}$, $l = 0, \ldots, 7$, see Figure 5. In particular, the choice of positions yields a parabolic scaling of the grids with the relationship length $\approx 2^{-j/2}$ and width $\approx 2^{-j}$.

As for the continuous transform, we define now the scaled windows in polar coordinates

$$U_j(r, \omega) := 2^{-3j/4} W(2^{-j} r) V \left(\frac{2 \cdot 2^{\lceil j/2 \rceil} \omega}{\pi} \right) = 2^{-3j/4} W(2^{-j} r) V \left(\frac{\omega}{\theta_{j,1}} \right), \qquad j \in \mathbb{N}_0. \quad (7)$$

The basic curvelet is defined by

$$\widehat{\phi}_{j,0,0}(\xi) := U_j(\xi),$$

and the family of curvelet functions is given by

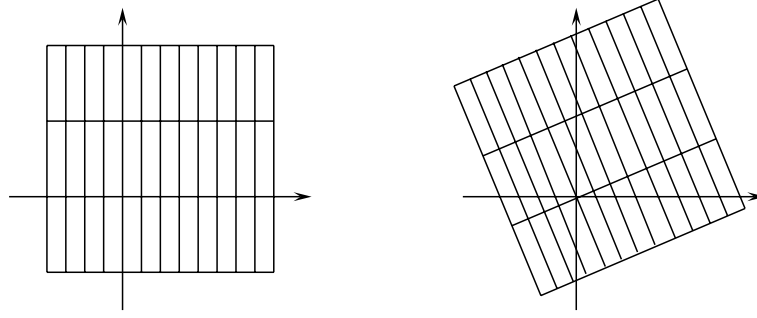$$\phi_{j,k,l}(x) := \phi_{j,0,0}(R_{\theta_{j,l}}(x - b_k^{j,l})). \quad (8)$$

11

Figure 5: Grid for $\theta_{4,0} = 0$ and for $\theta_{4,1} = \pi/8$.

In frequency domain, the curvelet functions

$$\widehat{\phi}_{j,k,l}(\xi) = e^{-i\langle b_k^{j,l}, \xi\rangle} \, U_j(R_{\theta_{j,l}}\xi) = e^{-i\langle b_k^{j,l}, \xi\rangle} \, 2^{-3j/4} \, W(2^{-j}r) V\left(\frac{\omega + \theta_{j,l}}{\theta_{j,1}}\right)$$

are supported inside the polar wedge with radius $2^{j-1} \leq r \leq 2^{j+1}$ and angle $\frac{2^{-\lceil j/2\rceil}\pi(-1-l)}{2} < \omega < \frac{2^{-\lceil j/2\rceil}\pi(1-l)}{2}$. The support of $\widehat{\phi}_{j,k,l}$ does not depend on the position $b_k^{j,l}$. For example, $\widehat{\phi}_{2,k,l}(r,\omega)$ is supported inside the wedge with $2 \leq r \leq 8$ and $\frac{(-1-l)\pi}{4} \leq \omega \leq \frac{(1-l)\pi}{4}$, $l = 0,\ldots,7$, see Figure 6. (Here we have used supp $V \subset [-1,1]$ and supp $W \subset [1/2,2]$.)
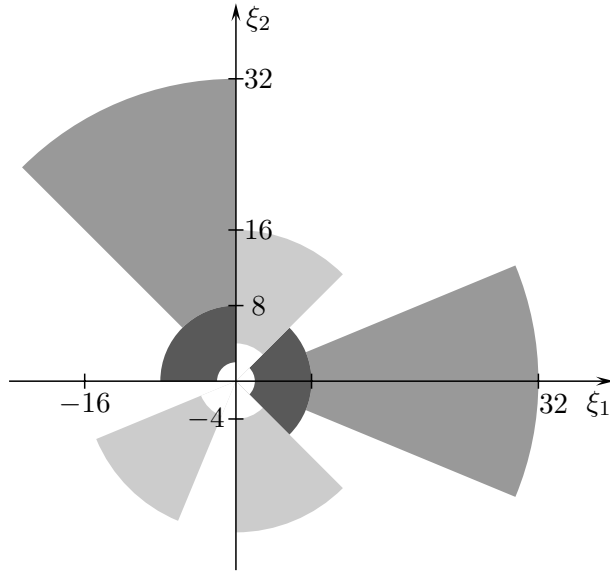

Figure 6: Maximal supports of $\widehat{\phi}_{2,k,0}$ and $\widehat{\phi}_{2,k,5}$(dark grey); of $\widehat{\phi}_{3,k,3}$, $\widehat{\phi}_{3,k,6}$ and $\widehat{\phi}_{3,k,13}$ (light grey); and of $\widehat{\phi}_{4,k,0}$ and $\widehat{\phi}_{4,k,11}$ (grey).

We again need some coarse scale curvelet elements for low frequencies and take here

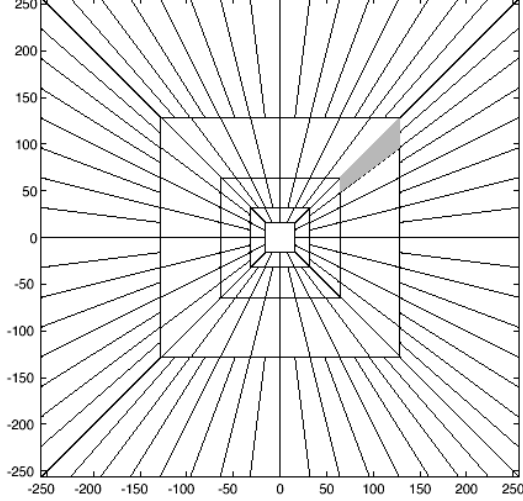$$\phi_{-1,k,0}(x) := \phi_{-1}(x - k), \qquad k \in \mathbb{Z}^2,$$

12

Figure 7: Discrete curvelet tiling with parabolic pseudo-polar support in the frequency plane.

where

$$\widehat{\phi}_{-1}(\xi) := W_0(|\xi|) \quad \text{with} \quad W_0(r)^2 := 1 - \sum_{j \geq 0} W(2^{-j}r)^2.$$

The system of curvelets

$$\{\phi_{-1,k,0} : k \in \mathbb{Z}^2\} \cup \{\phi_{j,k,l} : j \in \mathbb{N}_0,\, l = 0, \ldots, 4 \cdot 2^{\lceil j/2 \rceil} - 1,\, k = (k_1, k_2)^T \in \mathbb{Z}^2\}$$

satisfies a **tight frame property**. Every function $f \in L^2(\mathbb{R}^2)$ can be represented as a curvelet series, that means, the discrete curvelet transform is invertible. We have

$$f = \sum_{j,k,l} \langle f, \phi_{j,k,l} \rangle \, \phi_{j,k,l}, \tag{9}$$

and the Parseval identity

$$\sum_{j,k,l} |\langle f, \phi_{j,k,l} \rangle|^2 = \|f\|^2_{L^2(\mathbb{R}^2)}, \quad \forall f \in L^2(\mathbb{R}^2)$$

holds. For a proof we refer to [12]. The terms $c_{j,k,l}(f) := \langle f, \phi_{j,k,l} \rangle$ are called **curvelet coefficients**. In particular, we obtain by Plancherel's Theorem for $j \geq 0$

$$
\begin{aligned}
c_{j,k,l}(f) \quad &:= \quad \int_{\mathbb{R}^2} f(x) \, \overline{\phi_{j,k,l}(x)} \, dx = \int_{\mathbb{R}^2} \widehat{f}(\xi) \, \overline{\widehat{\phi}_{j,k,l}(\xi)} \, d\xi \\
&= \quad \int_{\mathbb{R}^2} \widehat{f}(\xi) \, U_j(R_{\theta_{j,l}} \xi) \, e^{i \langle b_k^{j,l}, \xi \rangle} \, d\xi. \tag{10}
\end{aligned}
$$

5.2 Transition to Cartesian arrays

In practical implementations one would like to have Cartesian arrays instead of the polar tiling of the frequency plane. Cartesian coronae are based on concentric squares (instead of circles) and shears, see Figure 7. Therefore, a construction of window functions on trapezoids instead

13

of polar wedges is desirable. Hence, we need to adapt the discrete curvelet system in Subsection 5.1 suitably. Let us remark that the frequency tiling into shears, as given in Figure 7, has been similarly used for the construction of contourlets [24] by a pyramidal directional filter bank. However, the tiling for the contourlet transform is slightly more flexible by allowing that the number of directions need not to be doubled at each scale, see [24].

We consider now the window function

$$\gamma(r) := \begin{cases} 1 & |r| \leq 1/2, \\ \cos \frac{(2|r|-1)\pi}{2} & 1/2 < |r| \leq 1, \\ 0 & \text{else,} \end{cases}$$

such that supp $\gamma = [-1, 1]$. As in [8], we replace the window $W_j(r) := W(2^{-j}r)$ in Subsection 4.1 by a window of the form

$$\widetilde{W}_j(r) := \chi_{[0,\infty)}(r) \cdot \sqrt{\gamma^2(2^{-j-1}r) - \gamma^2(2^{-j}r)}, \qquad j \geq 0, \, r \geq 0.$$

Hence supp $\widetilde{W}_j = [2^{j-1}, 2^{j+1}]$. Further, for $\xi_1 > 0$, let $V_j(\xi) := V(2^{\lfloor j/2 \rfloor} \xi_2/\xi_1)$ with V in Subsection 4.1, such that the support of V_j is inside the cone

$$K_1 := \{(\xi_1, \xi_2) : \xi_1 > 0, \, \xi_2 \in [-2\xi_1/3, 2\xi_1/3]\}.$$

Here, $\lfloor x \rfloor$ denotes the largest integer being smaller than or equal to x. Now, the Cartesian window,

$$\widetilde{U}_j(\xi) := 2^{-3j/4} \widetilde{W}_j(\xi_1) V_j(\xi) = 2^{-3j/4} \widetilde{W}_j(\xi_1) V \left(\frac{2^{\lfloor j/2 \rfloor} \xi_2}{\xi_1} \right)$$

can be defined, being analogous to U_j in (7) and determining the frequencies in the trapezoid

$$\{(\xi_1, \xi_2) : 2^{j-1} \leq \xi_1 \leq 2^{j+1}, \, -2^{-\lfloor j/2 \rfloor} \cdot \frac{2}{3} \leq \xi_2/\xi_1 \leq 2^{-\lfloor j/2 \rfloor} \cdot \frac{2}{3}\}.$$

The window $\widetilde{U}_0$ is presented in Figure 8. It is the Cartesian equivalent of U_0 ($= U_a$ with $a = 1$ in the notation of Subsection 4.1) in Figure 3.

Next, instead of equidistant angles, we define a set of equispaced slopes in the eastern cone $K = \{(\xi_1, \xi_2)^T : \xi_1 > 0, \, -\xi_1 < \xi_2 \leq \xi_1\}$,

$$\tan \theta_{j,l} := l \, 2^{-\lfloor j/2 \rfloor}, \qquad l = -2^{\lfloor j/2 \rfloor} + 1, \ldots, 2^{\lfloor j/2 \rfloor} - 1.$$

Observe that the angles $\theta_{j,l}$, which range between $-\pi/4$ and $\pi/4$, are not equispaced here, while the slopes are.

Now, let the curvelet-like functions be given by

$$\begin{aligned} \widehat{\widetilde{\phi}}_{j,0,0} &:= \widetilde{U}_j(\xi), \\ \widetilde{\phi}_{j,k,l}(x) &:= \widetilde{\phi}_{j,0,0}\left(S_{\theta_{j,l}}^T (x - \widetilde{b}_k^{j,l}) \right), \end{aligned} \tag{11}$$

being the Cartesian counterpart of $\phi_{j,k,l}$ in (8), with the shear matrix

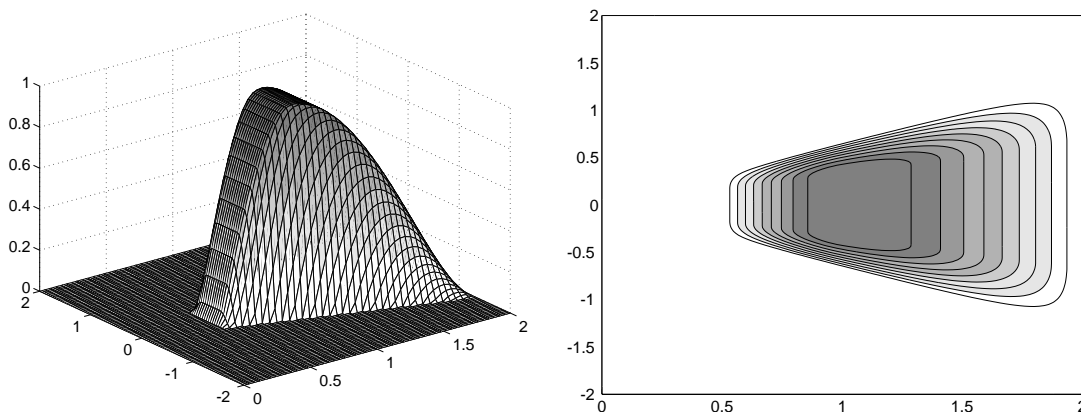$$S_\theta = \begin{pmatrix} 1 & 0 \\ -\tan \theta & 1 \end{pmatrix},$$

14

Figure 8: Window $\tilde{U}_0(\xi)$ (left) and its support (right).

and where $\widetilde{b}_k^{j,l} := S_{\theta_{j,l}}^{-T}(k_1\, 2^{-j},\, k_2\, 2^{-\lfloor j/2 \rfloor}) =: S_{\theta_{j,l}}^{-T} k_j$. Let us have a closer look at the functions $\widetilde{\phi}_{j,k,l}$. The Fourier transform gives by $S_{\theta_{j,l}}^{-1}\xi = (\xi_1, \xi_1 \tan\theta_{j,l} + \xi_2)^T$

$$
\begin{aligned}
\widehat{\widetilde{\phi}}_{j,k,l}(\xi) &= e^{-i\langle \widetilde{b}_k^{j,l}, \xi \rangle}\, \widehat{\widetilde{\phi}}_{j,0,0}(S_{\theta_{j,l}}^{-1}\xi) = e^{-i\langle \widetilde{b}_k^{j,l}, \xi \rangle}\, \widetilde{U}_j(S_{\theta_{j,l}}^{-1}\xi) \\
&= e^{-i\langle \widetilde{b}_k^{j,l}, \xi \rangle}\, 2^{-3j/4} \widetilde{W}_j(\xi_1)\, V_j(S_{\theta_{j,l}}^{-1}\xi) = e^{-i\langle \widetilde{b}_k^{j,l}, \xi \rangle}\, 2^{-3j/4} \widetilde{W}_j(\xi_1)\, V(2^{\lfloor j/2 \rfloor}\xi_2/\xi_1 + l).
\end{aligned}
$$

Hence, $\widehat{\widetilde{\phi}}_{j,k,l}$ is compactly supported on sheared trapezoids.

Let us for example examine $\widehat{\widetilde{\phi}}_{4,k,l}$. For $j = 4$, we consider the angles $\tan\theta_{4,l} = l/4$, $l = -3, \ldots, 3$. The support of $\widehat{\widetilde{\phi}}_{j,0}$ is symmetric with respect to the ξ_1 axis, and for $j = 4$ we have

$$
\operatorname{supp} \widehat{\widetilde{\phi}}_{4,k,0} = \{(\xi_1, \xi_2)^T : 8 \le \xi_1 \le 32,\ -\frac{1}{6} \le \frac{\xi_1}{\xi_2} \le \frac{1}{6}\}.
$$

The supports of $\widehat{\widetilde{\phi}}_{4,k,l}$ with $l = -3, \ldots, 3$ are now sheared versions of this trapezoid, see Figure 9.

The set of curvelets $\widetilde{\phi}_{j,k,l}$ in (11) needs to be completed by symmetry and by rotation by $\pm\pi/2$ radians in order to obtain the whole family. Moreover, as we can also see in Figure 9, we need suitable "corner elements" connecting the four cones (north, west, south, east). In [8], it is suggested to take a corner element as the sum of two half-part sheared curvelet functions of neighboring cones as indicated in Figure 9 (left). More precisely, we take

$$
\widehat{\widetilde{\phi}}_{j,0,-2^{\lfloor j/2 \rfloor}}(\xi) := 2^{-3j/4} W_j(\xi_1) V^h\left(2^{\lfloor j/2 \rfloor}\left(1 + \frac{\xi_2}{\xi_1}\right)\right) + 2^{-3j/4} W_j(\xi_2) V^h\left(2^{\lfloor j/2 \rfloor}\left(1 - \frac{\xi_1}{\xi_2}\right)\right),
$$

where the window function $V^h(t) := V(t)\,\chi_{[-1,0]}(t)$ is the left part of the window V and has only the half support $[-2/3,\, 0]$.

Finally, the coarse curvelet elements for low frequencies are needed, and we take here

$$
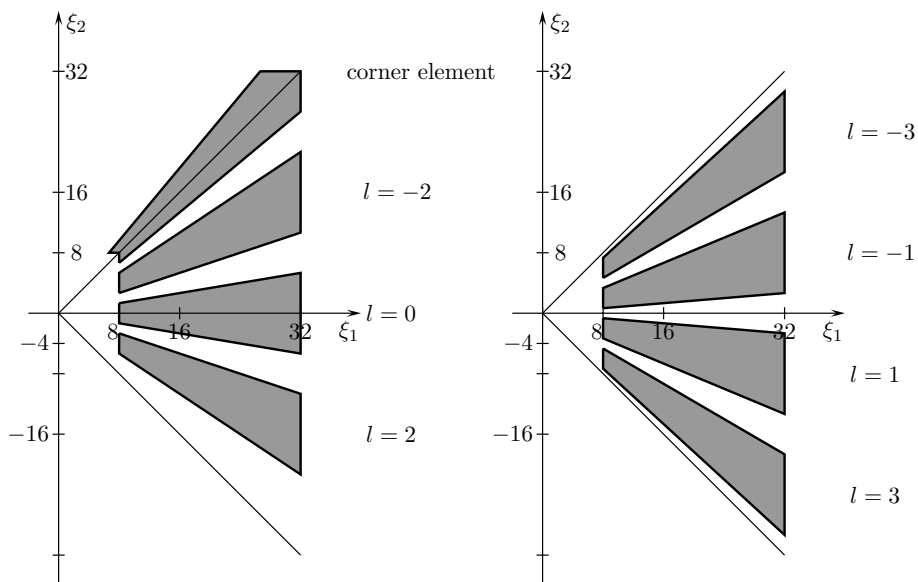\widetilde{\phi}_{-1,k,0}(x) := \widetilde{\phi}_{-1}(x - k), \qquad k \in \mathbb{Z}^2
$$

15

Figure 9: Supports of the functions $\widehat{\widetilde{\phi}}_{4,k,l}$ for $l = -3, \ldots, 3$, and one corner element.

with $\widehat{\widetilde{\phi}}_{-1}(\xi) := \gamma(\xi_1)\,\gamma(\xi_2)$. For this construction of curvelet-like elements one can show that

$$\widehat{\widetilde{\phi}}_{-1}(\xi) + \sum_{j=0}^{\infty} \sum_{l=-2^{\lfloor j/2 \rfloor}}^{2^{\lfloor j/2 \rfloor}} 2^{3j/4} \widehat{\widetilde{\phi}}_{j,0,l}(\xi) = 1$$

for all ξ in the eastern cone $K = \{(\xi_1, \xi_2)^T : \xi_1 > 0, \xi_2 \in [-\xi_1, \xi_1]\}$, where we have taken also the two corner elements in the sum. Similarly, this assertion is true for the rotated functions in the other three cones.

5.3 The algorithm

We find the Cartesian counterpart of the coefficients in (10) by

$$
\begin{aligned}
\widetilde{c}_{j,k,l}(f) &= \langle f, \widetilde{\phi}_{j,k,l} \rangle = \int_{\mathbb{R}^2} \widehat{f}(\xi)\, \widetilde{U}_j(S_{\theta_{j,l}}^{-1}\xi)\, e^{i\langle \widetilde{b}_k^{j,l}, \xi \rangle} d\xi \\
&= \int_{\mathbb{R}^2} \widehat{f}(S_{\theta_{j,l}}\xi)\, \widetilde{U}_j(\xi)\, e^{i\langle k_j, \xi \rangle} d\xi
\end{aligned}
\tag{12}
$$

with $k_j = (k_1 2^{-j},\, k_2 2^{-\lfloor j/2 \rfloor})^T$, $(k_1, k_2)^T \in \mathbb{Z}^2$.

The forward and the inverse Fast Discrete Curvelet Transform as presented in [8] and in CurveLab have a computational cost of $\mathcal{O}(N^2 \log N)$ for an $(N \times N)$ image, see http:curvelab.org with a collection of Matlab and C++ programs. The redundancy of that curvelet transform implementation is about 2.8 when wavelets are chosen at the finest scale, and 7.2 otherwise (see e.g. [8]). Using formula (12), the forward algorithm has roughly the following form.

1. **Compute the Fourier transform of f by means of a $2D$ FFT.**
   Let f be given by its samples $f(\frac{n_1}{N}, \frac{n_2}{N})$, $n_1, n_2 = 0, \ldots, N-1$, where N is of the form $N = 2^J$, $J \in \mathbb{N}$. Suppose, that f can be approximated by a linear combination of bivariate hat functions. Let $\tilde{s}(x) = s(x_1)\,s(x_2)$ with $s(x_1) := (1 - |x_1|)\,\chi_{[-1,1]}(x_1)$ and

$$f(x) = \sum_{n_1=0}^{N-1} \sum_{n_2=0}^{N-1} f\left(\frac{n_1}{N}, \frac{n_2}{N}\right) \tilde{s}(Nx_1 - n_1,\, Nx_2 - n_2).$$

With $\widehat{\tilde{s}}(\xi) = (\operatorname{sinc} \xi_1/2)^2\,(\operatorname{sinc} \xi_2/2)^2$ it follows that

$$\widehat{f}(\xi) = \sum_{n_1=0}^{N-1} \sum_{n_2=0}^{N-1} f\left(\frac{n_1}{N}, \frac{n_2}{N}\right) e^{-i(n_1\xi_1 + n_2\xi_2)/N}\, \widehat{\tilde{s}}\left(\frac{\xi}{N}\right),$$

and the 2D FFT of length N gives us the samples $\widehat{f}(2\pi n_1, 2\pi n_2)$, $n_1, n_2 = -\frac{N}{2}, \ldots, \frac{N}{2} - 1$.

2. **Compute $\widehat{f}(S_{\theta_{j,l}}\xi)$ by interpolation.**
   Fix the scales to be considered, say $j_0 \le j \le J$. The support of $\widetilde{U}_j$ is contained in the rectangle $R_j = [2^{j-1}, 2^{j+1}] \times [-2^{\lfloor j/2 \rfloor}, 2^{\lfloor j/2 \rfloor}]$. For each pair (j, l) compute now $\widehat{f}(2\pi n_1, 2\pi n_2 - 2\pi n_1 \tan\theta_{j,l})$ for $2\pi(n_1, n_2) \in R_j$.

3. **Compute the product $\widehat{f}(S_{\theta_{j,l}}\xi)\,\widetilde{U}_j(\xi)$.**
   For each pair (j, l) compute the product $\widehat{f}(2\pi n_1, 2\pi n_2 - 2\pi n_1 \tan\theta_{j,l})\,\widetilde{U}_j(2\pi n_1, 2\pi n_2)$.

4. **Apply the inverse $2D$ FFT** in order to obtain the discrete coefficients $\widetilde{c}_{j,k,l}^D(f)$ that are an approximation of the coefficients in (12).

For the inverse curvelet transform, one applies the algorithm in each step in reversed order. Observe that in the second step a suitable approximation scheme has to be applied in the forward transform and in the inverse transform.

6   3D Curvelet transform

For three-dimensional data, a generalization to three-dimensional multiscale geometric methods is of great interest. So far, only a few papers have been concerned with applications of the three-dimensional curvelet transform to 3D turbulence [2, 53] and 3D seismic processing [59].

In this section, we develop the idea of the three-dimensional curvelet transform on Cartesian arrays analogously as done in Section 5.2 for the two-dimensional case. Using polar coordinates, we consider curvelet functions being supported on sheared truncated pyramids instead of sheared trapezoids. In contrast to [77], we introduce three-dimensional shear matrices. The three-dimensional curvelet functions depend on four indices instead of three; the scale, the position and two angles.

In $\mathbb{R}^3$ we denote with $x = (x_1, x_2, x_3)^T$ the spatial variable and with $\xi = (\xi_1, \xi_2, \xi_3)^T$ the variable in frequency domain. Again, we use polar coordinates $(r, \omega_1, \omega_2)^T$ with $r = \sqrt{\xi_1^2 + \xi_2^2 + \xi_3^2}$, $\sin \omega_1 = \xi_2/\sqrt{\xi_1^2 + \xi_2^2}$, $\omega_1 \in [0, 2\pi)$, and $\cos \omega_2 = \xi_3/r$, $\omega_2 \in [0, \pi]$.

As in the two-dimensional case, we define a pair of smooth, nonnegative, real-valued window functions. We consider the same window $\widetilde{W}_j(r)$ as in Section 5.2,

$$\widetilde{W}_j(r) := \chi_{[0,\infty)}(r) \cdot \sqrt{\gamma^2(2^{-j-1}r) - \gamma^2(2^{-j}r)}, \qquad j \geq 0, \, r \geq 0,$$

such that $\operatorname{supp} \widetilde{W}_j = [2^{j-1}, 2^{j+1}]$. Further, let

$$\widetilde{V}_j(\xi) := V\left(2^{\lfloor j/2 \rfloor} \frac{\xi_2}{\xi_1}\right) V\left(2^{\lfloor j/2 \rfloor} \frac{\xi_3}{\xi_1}\right)$$

with the window V as in Subsection 4.1. Obviously, $\widetilde{V}_j$ is supported in the cone $\{(\xi_1, \xi_2, \xi_3) : \xi_1 > 0, \xi_2 \in [-\frac{2}{3}\xi_1, \frac{2}{3}\xi_1], \xi_3 \in [-\frac{2}{3}\xi_1, \frac{2}{3}\xi_1]\}$. Disregarding the normalization constant, let the Cartesian window $\widetilde{U}_j$ be defined by

$$\widetilde{U}_j(\xi) = \widetilde{U}_j(\xi_1, \xi_2, \xi_3) = \widetilde{W}_j(\xi_1) \, \widetilde{V}_j(\xi) = \widetilde{W}_j(\xi_1) \, V\left(2^{\lfloor j/2 \rfloor} \frac{\xi_2}{\xi_1}\right) V\left(2^{\lfloor j/2 \rfloor} \frac{\xi_3}{\xi_1}\right),$$

determining the frequencies in the truncated pyramid

$$\{(\xi_1, \xi_2, \xi_3)^T : 2^{j-1} \leq \xi_1 \leq 2^{j+1}, -\tfrac{2}{3}2^{-\lfloor j/2 \rfloor} \leq \tfrac{\xi_2}{\xi_1} \leq \tfrac{2}{3}2^{-\lfloor j/2 \rfloor}, -\tfrac{2}{3}2^{-\lfloor j/2 \rfloor} \leq \tfrac{\xi_3}{\xi_1} \leq \tfrac{2}{3}2^{-\lfloor j/2 \rfloor}\}.$$

Every Cartesian corona has six components, one for each face of the unit cube. Let us consider only the cone

$$K = \left\{(\xi_1, \xi_2, \xi_3) : \xi_1 > 0, -1 \leq \frac{\xi_2}{\xi_1} < 1, -1 \leq \frac{\xi_3}{\xi_1} < 1\right\}.$$

With the angles

$$\begin{aligned}
\tan \theta_{j,l} &:= l \, 2^{-\lfloor j/2 \rfloor}, & l = -2^{\lfloor j/2 \rfloor} + 1, \dots, 2^{\lfloor j/2 \rfloor} - 1, \\
\tan \vartheta_{j,m} &:= m \, 2^{-\lfloor j/2 \rfloor}, & m = -2^{\lfloor j/2 \rfloor} + 1, \dots, 2^{\lfloor j/2 \rfloor} - 1,
\end{aligned}$$

we define the three-dimensional shear matrix

$$S_{\theta_{j,l}, \vartheta_{j,m}} := \begin{pmatrix} 1 & 0 & 0 \\ -\tan \theta_{j,l} & 1 & 0 \\ -\tan \vartheta_{j,m} & 0 & 1 \end{pmatrix}$$

and the positions

$$\widetilde{b}_k^{j,l,m} := S_{\theta_{j,l}, \vartheta_{j,m}}^{-T}(k_1 2^{-j}, k_2 2^{-\lfloor j/2 \rfloor}, k_3 2^{-\lfloor j/2 \rfloor})^T = S_{\theta_{j,l}, \vartheta_{j,m}}^{-T} k_j,$$

where $(k_1, k_2, k_3)^T \in \mathbb{Z}^3$. Now in the cone K the curvelet functions are given by

$$\begin{aligned}
\widehat{\widetilde{\phi}}_{j,0,0,0}(\xi) &:= \widetilde{U}_j(\xi), \\
\widetilde{\phi}_{j,k,l,m} &:= \widetilde{\phi}_{j,0,0,0}(S_{\theta_{j,l}, \vartheta_{j,m}}^T(x - \widetilde{b}_k^{j,l,m})).
\end{aligned}$$

This definition can be seen as a direct generalization of (11). The Fourier transform gives

$$\widehat{\widetilde{\phi}}_{j,k,l,m}(\xi) = e^{-i\langle \widetilde{b}_k^{j,l,m}, \xi \rangle} \widehat{\widetilde{\phi}}_{j,0,0,0}(\xi)$$

$$= e^{-i\langle \widetilde{b}_k^{j,l,m}, \xi \rangle} \widetilde{W}_j(\xi_1) V\left(2^{\lfloor j/2 \rfloor} \frac{\xi_2}{\xi_1} + l\right) V\left(2^{\lfloor j/2 \rfloor} \frac{\xi_3}{\xi_1} + m\right),$$

i.e., the functions $\widehat{\widetilde{\phi}}_{j,k,l,m}$ are compactly supported on sheared truncated pyramids (see e.g. Figure 3 in [77]). As in the two-dimensional case one needs to take care for special boundary elements where two (or three) different cones touch each other.

(a)   (b)   (c)

(d)   (e)   (f)
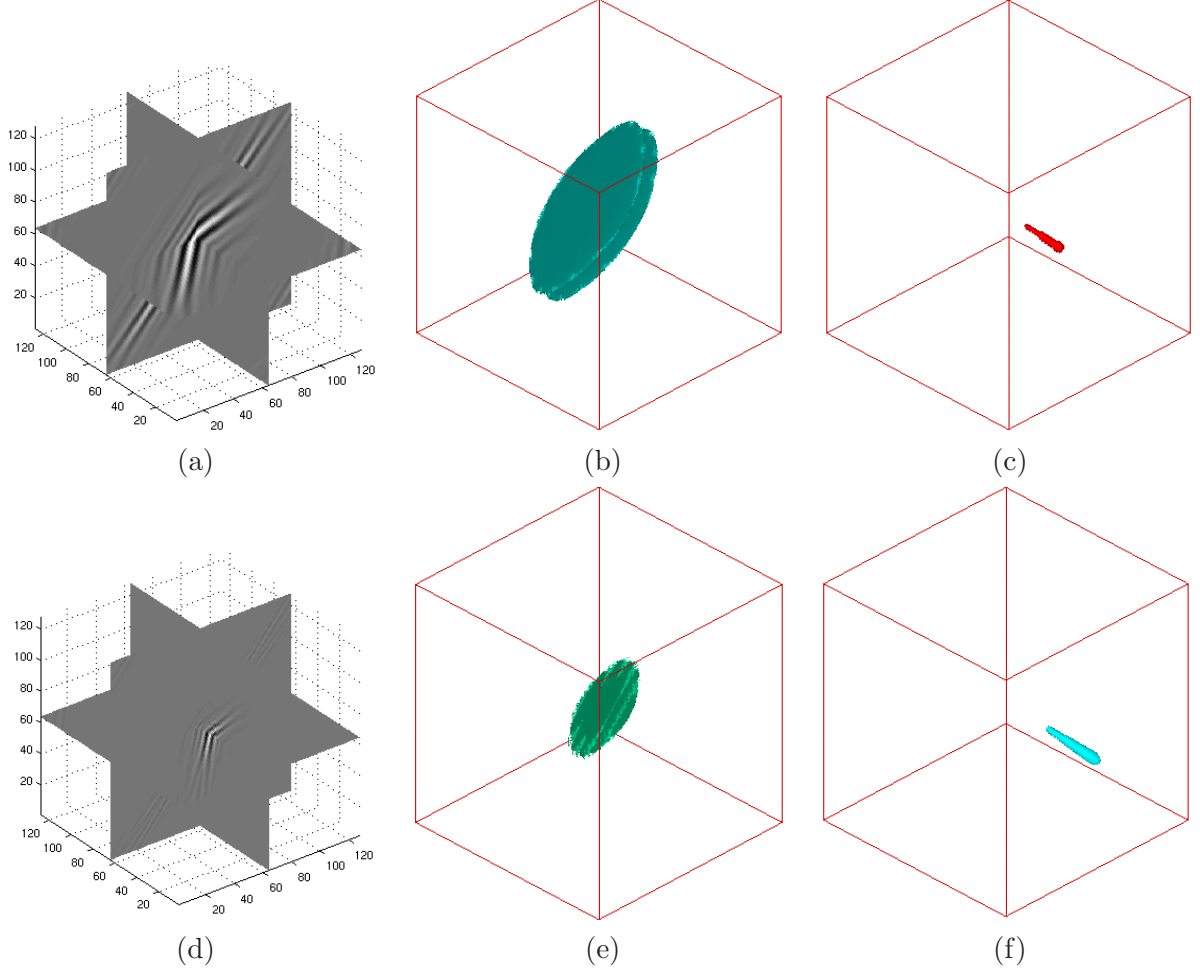
Figure 10: An element of 3D curvelets at a coarser scale (upper row) and finer scale (lower row) is shown in three cross-sections (left column) and isosurface (middle column). The right column shows their frequency support. It can be clearly seen that the element with high resolution in the space domain has low resolution in the frequency domain.

Figure 10 shows some 3D curvelet elements. Observe that in the spatial domain, $\phi_{j,k,l,m}$ is of plate-like shape, which rapidly decays away from a 2^{-j} by $2^{-j/2}$ cross-section rectangle with center $\widetilde{b}_k^{(j,l,m)}$ and orientations $\theta_{j,l}$ (with respect to the horizontal axis in x) and $\vartheta_{j,m}$ (with respect to the vertical axis in x). The element is smooth within the plate but exhibits oscillating

decay in the normal direction of the plate. It obeys a parabolic scaling law between the thickness and length (thickness $\approx$ length^2) and directional sensitivity (Orientations $= 1/\sqrt{\text{scale}}$).

As always, for the coarsest scale we need a special construction, as e.g.

$$\widetilde{\phi}_{-1,k}(x) := \widetilde{\phi}_{-1}(x-k), \qquad k \in \mathbb{Z}^3$$

with $\widehat{\widetilde{\phi}}_{-1}(\xi) := \gamma(\xi_1)\,\gamma(\xi_2)\,\gamma(\xi_3)$, where γ is defined in Subsection 5.2.

Analogously as in (12), the curvelet coefficients are given by

$$
\begin{aligned}
\widetilde{c}_{j,k,l,m}(f) &= \langle f, \widetilde{\phi}_{j,k,l,m}\rangle = \int_{\mathbb{R}^3} \widehat{f}(\xi)\,\widetilde{U}_j(S^{-1}_{\theta_{j,l},\vartheta_{j,m}}\xi)\,e^{i\langle \widetilde{b}_k^{j,l,m},\xi\rangle}\,d\xi \\
&= \int_{\mathbb{R}^3} \widehat{f}(S_{\theta_{j,l},\vartheta_{j,m}}\xi)\,\widetilde{U}_j(\xi)\,e^{i\langle k_j,\xi\rangle}d\xi.
\end{aligned}
$$

An algorithm can now be derived similarly as in Subsection 5.3 for the two-dimensional case. The computational complexity of the three-dimensional discrete curvelet transform based on FFT algorithms is $\mathcal{O}(n^3 \log n)$ flops for $n \times n \times n$ data [8]. For further details we refer to [8] and [77].

7 RECENT APPLICATIONS

In this section, we shall review applications of the curvelets in image processing, seismic exploration, fluid mechanics, solving of PDEs, and compressed sensing, to show their potential as an alternative to wavelet transforms in some scenarios.

7.1 Image processing

In 2002, the first-generation curvelet transform was applied for the first time to image denoising by Starck et al. [69], and by Candès and Guo [14]. The applications of the first-generation curvelets were extended to image contrast enhancement [71] and astronomical image representation [70] in 2003, and to fusion of satellite images [19] in 2005. After the effective second-generation curvelet transform [13] had been proposed in 2004, the applications of curvelets increased very fast in many fields involving image/video presentation, denoising and classification. For instance, Ma et al. applied the second-generation curvelets for motion estimation and video tracking of geophysical flows [50], surface characterization [47] and deblurring [48]. Ma and Plonka presented two different models for image denoising by combining the discrete curvelet transform with nonlinear diffusion schemes. In the first model [55], a curvelet shrinkage is applied to the noisy data, and the result is further processed by a projected total variation diffusion in order suppress pseudo-Gibbs artifacts. In the second model [64], a nonlinear reaction-diffusion equation is applied, where curvelet shrinkage is used for regularization of the diffusion process. Starck et al. [72, 3] applied curvelets for morphological component analysis. Recently, B. Zhang et al. [78] used curvelets for Poisson noise removal in comparison with wavelets and ridgelets. In [79], C. Zhang et al. successively applied the multiscale curvelet transform to multipurpose watermarking for content authentication and copyright verification. Jiang et al. [40] considered structure and texture image inpainting with the help of an iterative curvelet thresholding method. Tessens et al. [75] proposed a new context adaptive image denoising by modeling of curvelet domain statistics. By performing an inter-sub-band statistical analysis of

curvelet coefficients, one can distinguish between two classes of coefficients: those that represent useful image content, and those dominated by noise. Using a prior model based on marginal statistics, an appropriate local spatial activity indicator for curvelets has been developed that is found to be very useful for image denoising, see [75]. Geback et al. [34] applied the curvelets for edge detection in microscopy images.

Interestingly, the pure discrete curvelet transform is less suitable for image compression and for image denoising. The reason may be the redundancy of the curvelet frame. Most successful approaches related with the discrete curvelet transform are hybrid methods, where curvelets are combined with another technique for image processing. These methods usually can exploit the ability of the curvelet transform to represent curve-like features.

Let us give one example of image denoising [55], where curvelet shrinkage is combined with nonlinear anisotropic diffusion. Figure 11 (a) shows a part of noisy Barbara image. Figures 11 (b)-(f) present the denoising results by using tensor-product Daubechies's DB4 wavelets, TV diffusion, contourlets, curvelets, and TV-combined curvelet transform [55], respectively. The curvelet-based methods preserve the edges and textures well.

7.2   Seismic processing

Seismic data records the amplitudes of transient/reflecting waves during receiving time. The amplitude function of time is called seismic trace. A seismic data or profile is the collection of these traces. All the traces together provide a spatio-temporal sampling of the reflected wave field containing different arrivals that respond to different interactions of the incident wave field with inhomogeneities in the Earth's subsurface. Common denominators among these arrivals are wave fronts (as shown in Fig. 12 (a) for a real seismic profile), which display anisotropic line-like features, as edges and textures in images. They basically show behaviors of C^2-continuous curves. The main characteristic of the wave fronts is their relative smoothness in the direction along the fronts and their oscillatory behavior in the normal direction. A crucial problem in seismic processing is to preserve the smoothness along the wave fronts when one aims to remove noise.

From a geophysical point of view, curvelets can be seen as local plane waves. They are optimal to sparsely represent the local seismic events and can be effectively used for wave front-preserving seismic processing. Therefore, the curvelet decomposition is an appropriate tool for seismic data processing.

Fig. 12 shows a denoising of a real seismic data set by curvelets, in comparison to wavelets. Five decomposing levels are used in both transforms. Fig. 13 shows the comparison of subband reconstruction in the first three levels from coarse scale to fine scale. It can be seen clearly that the curvelets perform much better than wavelets to preserve the wave fronts/textures in multiscale decomposition and denoising. We also observe that the curvelet transform can achieve an almost complete data reconstruction if used without any thresholding for coefficients (reconstructed SNR = 310.47 and error = 2.9770e-010).

So far, curvelets have been applied successfully in seismic processing. Hennenfent and Herrmann [36] suggested a nonuniformly sampled curvelet transform for seismic denoising. Neelamani et al. [59] proposed a 3D curvelet-based effective approach to attenuate random and coherent noise in a 3D data set from a carbonate environment. Comparisons of wavelets, contourlets, curvelets, and their combination for denoising of random noise have been also investigated in [66]. Douma and de Hoop [28] presented a leading-order seismic imaging by curvelets
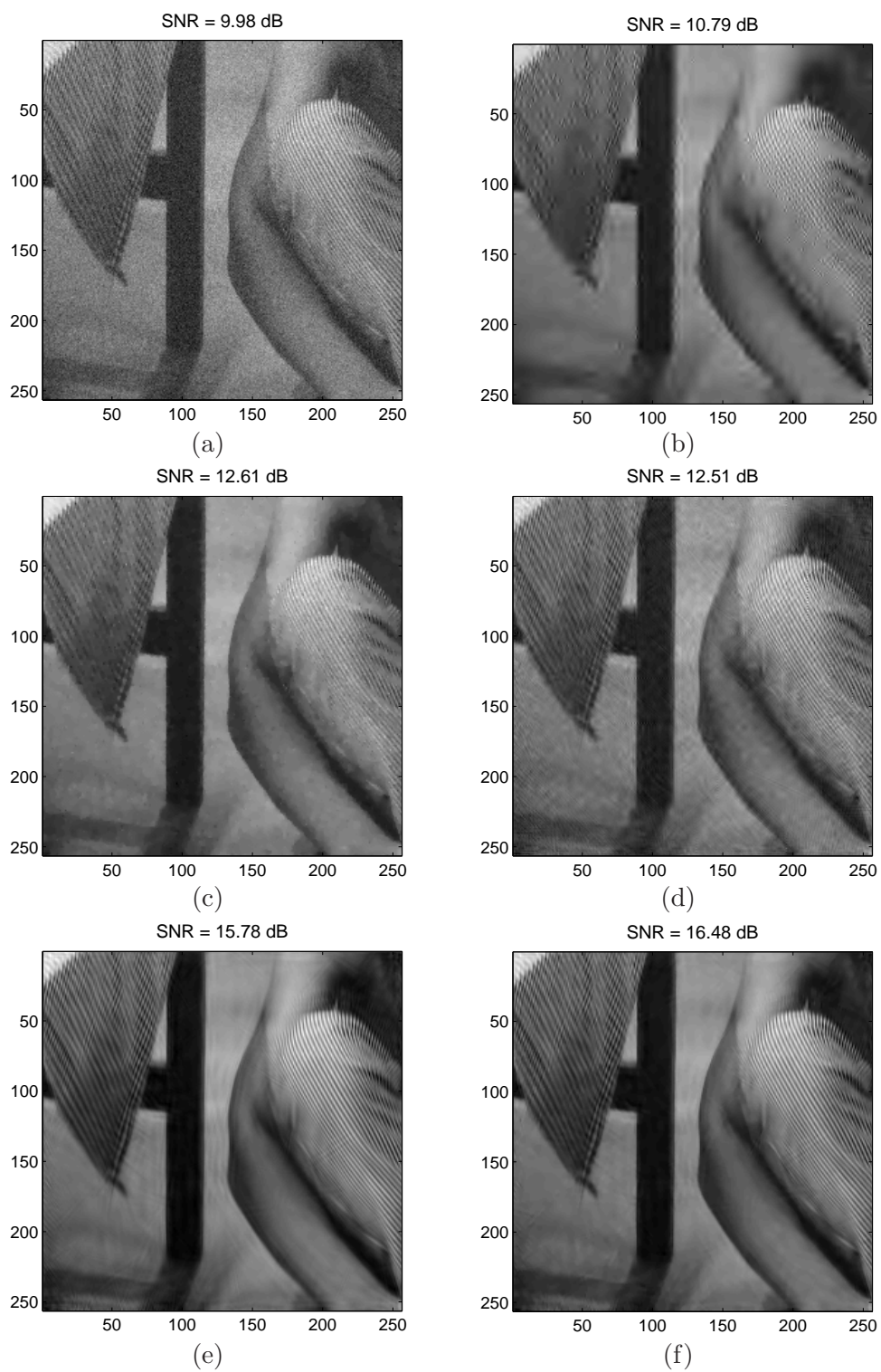
Figure 11: Image denoising. (a) Noisy image, (b) wavelet denoising, (c) TV-diffusion denoising, (d) contourlet denoising, (e) curvelet denoising, (f) TV-combined curvelet denoising.
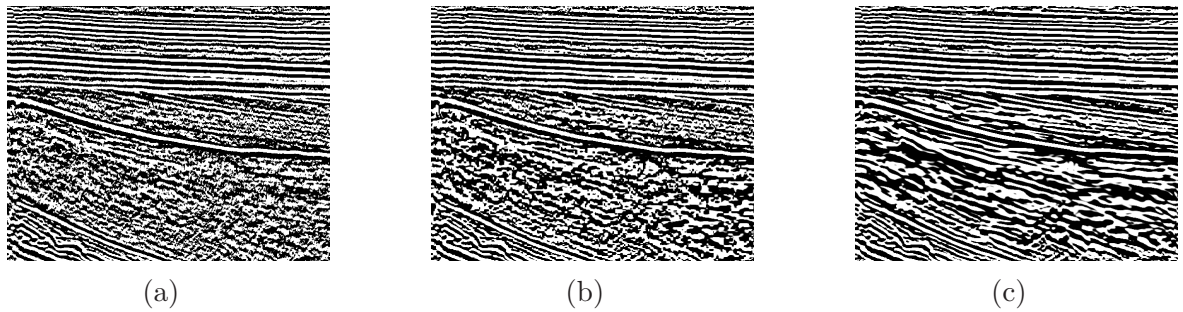
Figure 12: Comparison of seismic denoising. (a) Original data, (b) wavelet denoising, (c) curvelet denoising.

They show that using curvelets as building blocks of seismic data, the Kirchhoff diffraction stack can, to leading order in angular frequency, horizontal wavenumber, and migrated location, be rewritten as a map migration of coordinates of the curvelets in the data, combined with an amplitude correction. This map migration uses the local slopes provided by the curvelet decomposition of the data. Chauris and Nguyen [17], and Chauris and Ma [18] considered seismic demigration/migration in the curvelet domain. The migration consists of three steps: decomposition of the input seismic data (e.g., common offset sections) using the curvelet transform; independent migration of the curvelet coefficients; inverse curvelet transform to obtain the final depth migrated image. Currently, they concentrate on a ray-based type of prestack depth-migration (i.e., common-offset Kirchhoff depth migration) with respect to heterogeneous velocity models. It comes out that curvelets are almost invariant under the migration operations. The final objective is to be able to derive a formulation and build an efficient algorithm for the full waveform inversion in the curvelet domain.

In addition, curvelet-based primary-multiple separation [39], extrapolation [45], and seismic data recovery [38, 37, 74] have been also proposed by Herrmann et al..

7.3 Turbulence analysis in fluid mechanics

Turbulence has been a source of fascination for centuries, because most fluid flows occurring in nature, as well as in engineering applications, are turbulent. Fluid turbulence is a paradigm of multiscale phenomena, where the coherent structures evolve in an incoherent random background. Turbulence is difficult to approximate and analyze mathematically or to calculate numerically because of its range of spatial and temporal scales. The geometrical representation of flow structures might seem to be restricted to a well defined set of curves along which the data are singular. As a consequence, the efficient compression of a flow field with minimum loss of the geometric flow structures is a crucial problem in the simulation of turbulence. The development of appropriate tools to study vortex breakdown, vortex reconnection, and turbulent entrainment at laminar-turbulent interfaces, is imperative to enhance our understanding of turbulence. Such tools must capture the vortical structure and dynamics accurately to unravel the physical mechanisms underlying these phenomena.

Recently, the curvelets have been applied to study the non-local geometry of eddy structures and the extraction of the coherent vortex field in turbulent flows [2, 53, 54]. Curvelets start to influence the field of turbulence analysis and have the potential to upstage the wavelet representation of turbulent flows addressed in [30, 31]. The multiscale geometric property, implemented
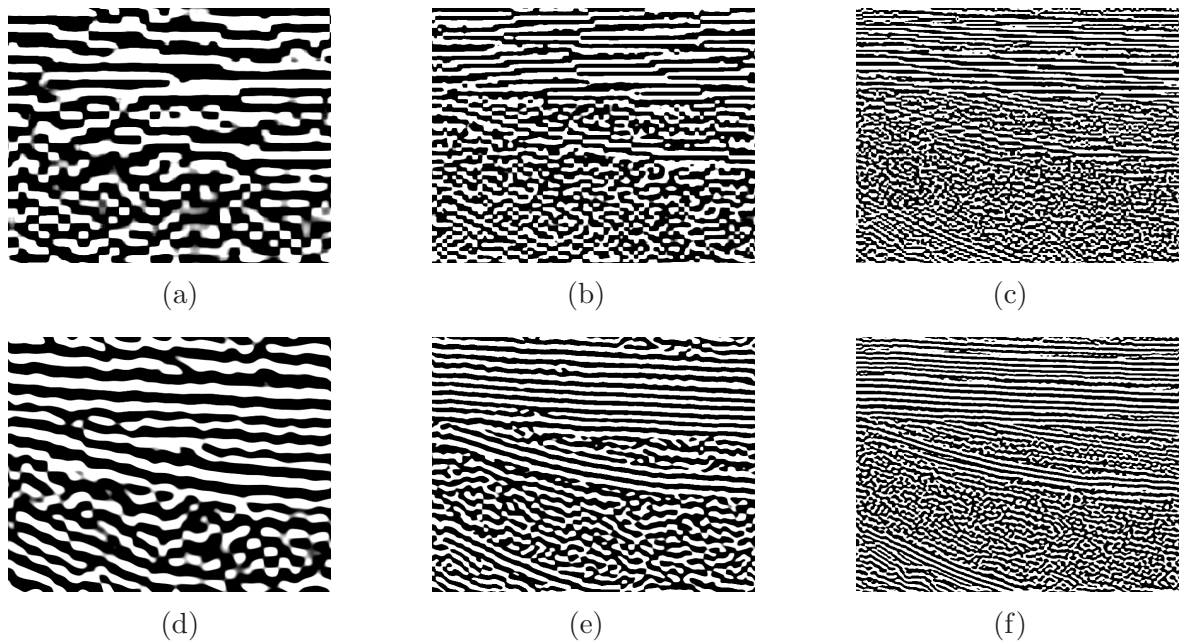
Figure 13: Comparisons of subband reconstruction in the first three levels from coarse scale to fine scale by wavelet transform (upper row) and curvelet transform (lower row).

by means of curvelets, provides the framework for studying the evolution of the structures associated to the main ranges of scales defined in Fourier space, while keeping the localization in physical space that enables a geometrical study of such structures. Such a geometrical characterization can provide a better understanding of cascade mechanics and dissipation-range dynamics. Moreover, curvelets have the potential to contribute to the development of structure-based models of turbulence fine scales, subgrid-scale models for large-eddy simulation, and simulation methods based on prior wavelet transforms [2].

Figure 14 gives an example for the extraction of coherent fields from turbulent flows. The curvelet method preserves the edges and structures better than wavelet methods. The results of multiscale turbulence analysis depend on the threshold or shrinkage. The question of how to find the optimal threshold to separate coherent fields and incoherent random fields still remains open.

7.4 Solving of PDEs

Candès and Demanet [6, 7] have shown that curvelets essentially provide optimally sparse representations of Fourier integral operators. While the wavelet transform is optimal for solving elliptical PDEs, the motivation to use the curvelet transform is that for a wide class of linear hyperbolic differential equations, the curvelet representation of the solution operator is both optimally sparse and well organized. Sparsity means that the matrix entries decay nearly exponentially fast, and they are well organized in the sense that very few nonnegligible entries occur near a few shifted diagonals. Wave fronts of solutions can be also sparsely represented in curvelet domain [7]. Some updated results for hyperbolic evolution equations with limited smoothness have been obtained by Andersson et al. [1]. The key idea of the existing methods is first to
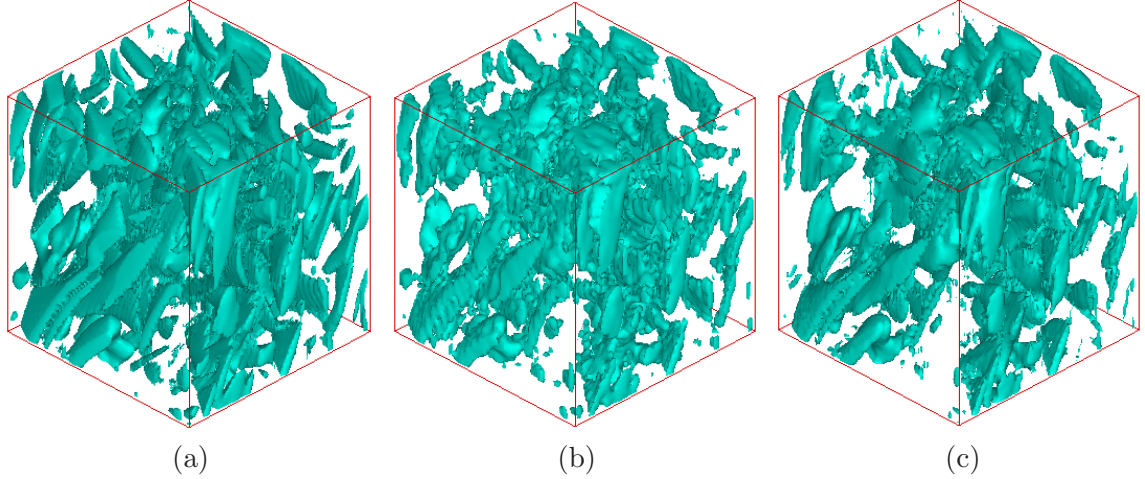
24

Figure 14: Extraction of coherent fields from turbulent flows. (a) Original flow, (b) coherent components by wavelets, and curvelets.

decompose the initial fields by the curvelet transform, and then to compute the rigid motions of the significant curvelet coefficients along Hamiltonian ray flows at each scale. Finally, one needs to reconstruct the evolution coefficients at all scales by an inverse curvelet transform and obtains an approximate wave field $u(x,t)$ at a given time t. The theory is quite elegant but still far away from practical applications. The papers cited above show the potential of curvelets for solving of PDEs from the point of view of mathematical analysis and raise the hope to achieve fast algorithms for the solution of hyperbolic PDEs using curvelets.

Let us consider a wave equation with the associated Cauchy initial value problem,

$$\frac{\partial^2 u}{\partial t^2}(x,t) = v^2 \, \Delta u(x,t) \quad u(x,0) = u_0(x), \quad \frac{\partial u}{\partial t}(x,0) = u_1(x). \tag{13}$$

For simplicity, assume that v is a constant wave speed, and $\Delta u(x,t) = \frac{\partial^2}{x_1^2} u(x,t) + \frac{\partial^2}{x_2^2} u(x,t)$ denotes the usual Laplace operator. Its solution can be written as $u(x,t) = F(x,t)u_0(x) + G(x,t)u_1(x)$, with suitable solution operators $F(x,t)$ and $G(x,t)$ (involving Green's functions) that can be sparsely represented in curvelet domain.

J. Ma and his students are working on curvelet-based finite difference schemes for seismic wave equations [56]. The goal is to construct a fast adaptive scheme for numerical modeling of wave propagation. Similarly as with prior wavelet-based finite difference schemes, one crucial problem is to explore how the differential operator Δ (or ∂_x) can be computed by the curvelet transform in an efficient way. The 2D wave field u can be transformed into curvelet domain by $u(x_1, x_2, t) = \sum_\mu c_\mu(t) \phi_\mu(x_1, x_2)$. Here, we have used the tight frame property (9) with the short notation $\mu = (j,k,l)$, and $c_\mu(t)$ denotes the μth curvelet coefficient of u at time t. A possible way to compute the curvelet coefficients of Δu is

$$c_\mu^\triangle := c_\mu(\Delta u) := \int \Delta u(x,t) \, \overline{\phi_\mu(x)} \, dx = \int \widehat{\Delta u}(\xi,t) \, \overline{\hat{\phi}_\mu(\xi)} \, d\xi = \int (-\xi_1^2 - \xi_2^2) \, \hat{u}(\xi,t) \, \overline{\hat{\phi}_\mu(\xi)} \, d\xi.$$

Using the definition of the curvelet coefficients in (12) we obtain with $S_{\theta_{j,l}}\xi = (\xi_1, -\xi_1 \tan \theta_{j,l} +$
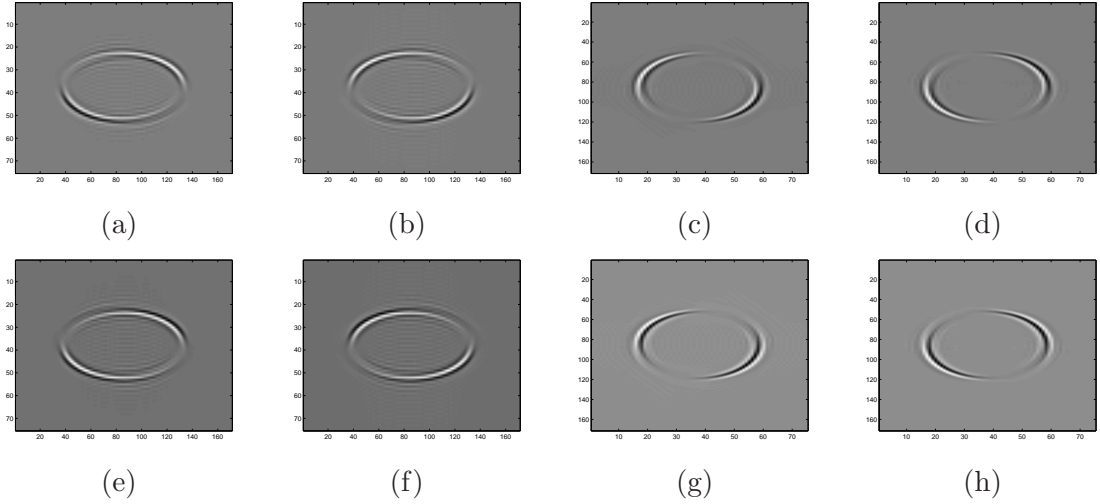
Figure 15: Curvelet coefficients of an instant wave field at the coarsest curvelet detail scale. (a)-(h) denotes eight different directional subbands in this curvelet scale.

$\xi_2)^T$

$$
\begin{aligned}
c_\mu^\triangle &= \int \left[-(1 + \tan^2 \theta_{j,l}) \xi_1^2 - \xi_2^2 + 2(\tan \theta_{j,l}) \xi_1 \xi_2 \right] \widehat{u}(S_{\theta_{j,l}} \xi) \, \widetilde{U}_j(\xi) \, e^{i\langle k_j, \xi \rangle} d\xi \\
&= 4^j (1 + \tan^2 \theta_{j,l}) \frac{\partial^2 c_\mu}{\partial k_1^2} + 4^{\lfloor j/2 \rfloor} \frac{\partial^2 c_\mu}{\partial k_2^2} - 2^{j+1} \, 2^{\lfloor j/2 \rfloor} \, \tan \theta_{j,l} \frac{\partial^2 c_\mu}{\partial k_1 \partial k_2}.
\end{aligned}
$$

Here we recall that $k = (k_1, k_2)^T \in \mathbb{Z}^2$ and $k_j = (k_1/2^j, \, k_2/2^{\lfloor j/2 \rfloor})^T$. That means, we can obtain the curvelet coefficients of Δu by using the coefficients of the instant wave field u. Thus, we can rewrite the wave equation in coefficient domain by

$$
\frac{\partial^2 c_\mu}{\partial t^2} = v^2 \left(4^j (1 + \tan^2 \theta_{j,l}) \frac{\partial^2 c_\mu}{\partial k_1^2} + 4^{\lfloor j/2 \rfloor} \frac{\partial^2 c_\mu}{\partial k_2^2} - 2^{j+1} \, 2^{\lfloor j/2 \rfloor} \tan \theta_{j,l} \frac{\partial^2 c_\mu}{\partial k_1 \partial k_2} \right). \tag{14}
$$

Figure 15 shows an example of curvelet coefficients of an instant wave field at the coarsest curvelet detail scale, by implementing the computation in curvelet domain as given in (14). For details of this approach we refer to [73]. Using a suitable thresholding, one can implement a fast adaptive computation for the wave propagation. Unfortunately, due to the redundancy of the current discrete curvelet algorithm, the curvelets have not performed at the level that we expected. The matrices are not as sparse as the estimates promise. The efficient numerical treatment of PDEs using curvelets is still a challenging problem.

7.5   Compressed sensing

Finally, we mention a new direction of applications of the curvelet transform to the so-called compressed sensing or compressive sampling (CS), an inverse problem with highly incomplete measurements. CS [15, 16, 25] is a novel sampling paradigm, which carries imaging and compression simultaneously. The CS theory says that a compressible unknown signal can be recovered by a small number of random measurements using sparsity-promoting nonlinear recovery algorithms. The number of necessary measurements is considerably smaller than the number of

needed traditional measurements that satisfy the Shannon/Nyquist sampling theorem, where the sampling rate has to be at least twice as large as the maximum frequency of the signal. The CS based data acquisition depends on its sparsity rather than its bandwidth. CS might have an important impact for designing of measurement devices in various engineering fields such as medical magnetic resonance (MRI) imaging and remote sensing, especially for cases involving incomplete and inaccurate measurements limited by physical constraints, or very expensive data acquisition.

Mathematically, we handle the fundamental problem of recovering a signal $x \in \mathbb{R}^N$ from a small set of measurements $y \in \mathbb{R}^K$. Let $A \in \mathbb{R}^{K \times N}$ be the so-called CS measurement matrix, where $K \ll N$, i.e., there are much fewer rows in the matrix than columns. The measurements can be described as [15]

$$y = Ax + \epsilon. \tag{15}$$

Here ϵ denotes possible measurement errors or noise. It seems to be hopeless to solve this ill-posed underdetermined linear system since the number of equations is much smaller than the number of unknown variables. However, if the x is compressible by a transform, as e.g. $x = T^{-1}c$, where T denotes the discrete curvelet transform, and the sequence of discrete curvelet coefficients $c = (c_\mu)$ is sparse, then we have $y = AT^{-1}c + \epsilon = \tilde{A}c + \epsilon$. If the measurement matrix A is not correlated with T, the sparse sequence of curvelet coefficients c can be recovered by a sparsity-constraint l_1-minimization [15],

$$\min_c \|y - \tilde{A}c\|_{l_2} + \lambda \|c\|_{l_1}.$$

The second term is a regularization term that represents the a-priori information of sparsity. To solve the minimization, an iterative curvelet thresholding (ICT) can be used, based on the Landweber descent method (see e.g. [37]),

$$c_{p+1} = S_\tau(c_p + \tilde{A}^T(y - \tilde{A}c_p)),$$

until $\|c_{p+1} - c_p\| < \varepsilon$, for a given error ε. Here the (soft) threshold function S_τ, given by

$$S_\tau(x) = \begin{cases} x - \tau, & x \geq \tau, \\ x + \tau, & x \leq -\tau, \\ 0, & |x| < \tau, \end{cases}$$

is taken componentwisely, i.e., for a sequence $a = (a_\mu)$ we have $S_\tau(a) = (S_\tau a_\mu)$.

Figure 16 shows an example of compressed sensing with 25 percent Fourier measurements. Here the operator A is obtained by a random subsampling of the Fourier matrix. Figure 16 (b) shows the 25% samples in Fourier domain, Figure 16 (c) is the recovering result by zero-filling reconstruction, and Figure 16 (d) is the result found by iterative curvelet thresholding. Figures 16 (e) and (f) denote the changes of the signal-to-noise ratio (SNR) and errors of the recovered images as the number of iterations increases. The unknown MRI image can be obtained by using highly incomplete measurements, which can reduce the on-line measurement time and thus lessen the pain of a patient.

The motivation of applying the curvelet thresholding method is that most natural images are compressible by the curvelet transform. Currently, a few researchers have applied the ICT method to compressed sensing in seismic data recovery [37, 38, 74], and remote sensing [49, 51]. Variant ICT methods (see e.g. [65]) have been also proposed for compressed sensing.
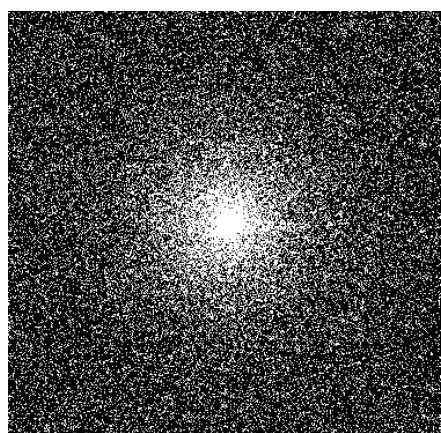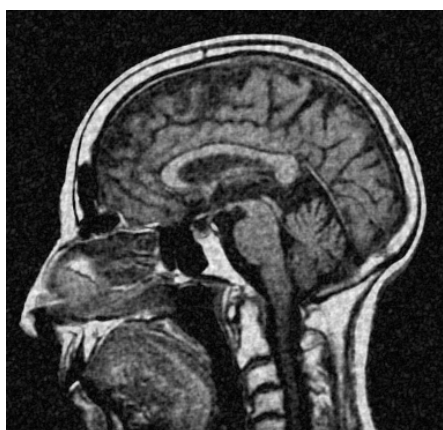
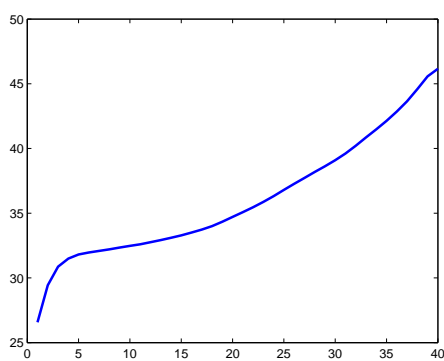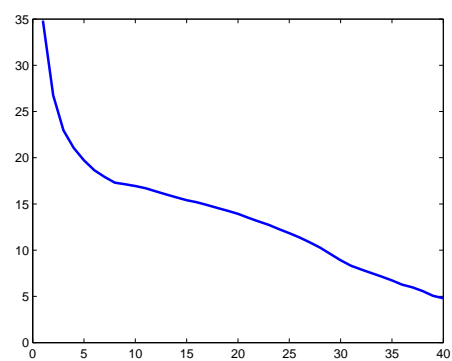Figure 16: Compressed sensing in Fourier domain for medical imaging. (a) Original MRI image, (b) pseudo-random Fourier sampling, (c) recovery by zero-filling reconstruction, (d) recovery by ICT, (e) SNR (in dB) of the recovered image vs number of iterations for the ICT, (f) recovery error vs number of iterations for the ICT.

Figure 17 shows an example for the curvelet-based compressed sensing in remote sensing [49, 51]. It can be seen that the curvelet method is superior to the wavelet method to recover the edges.
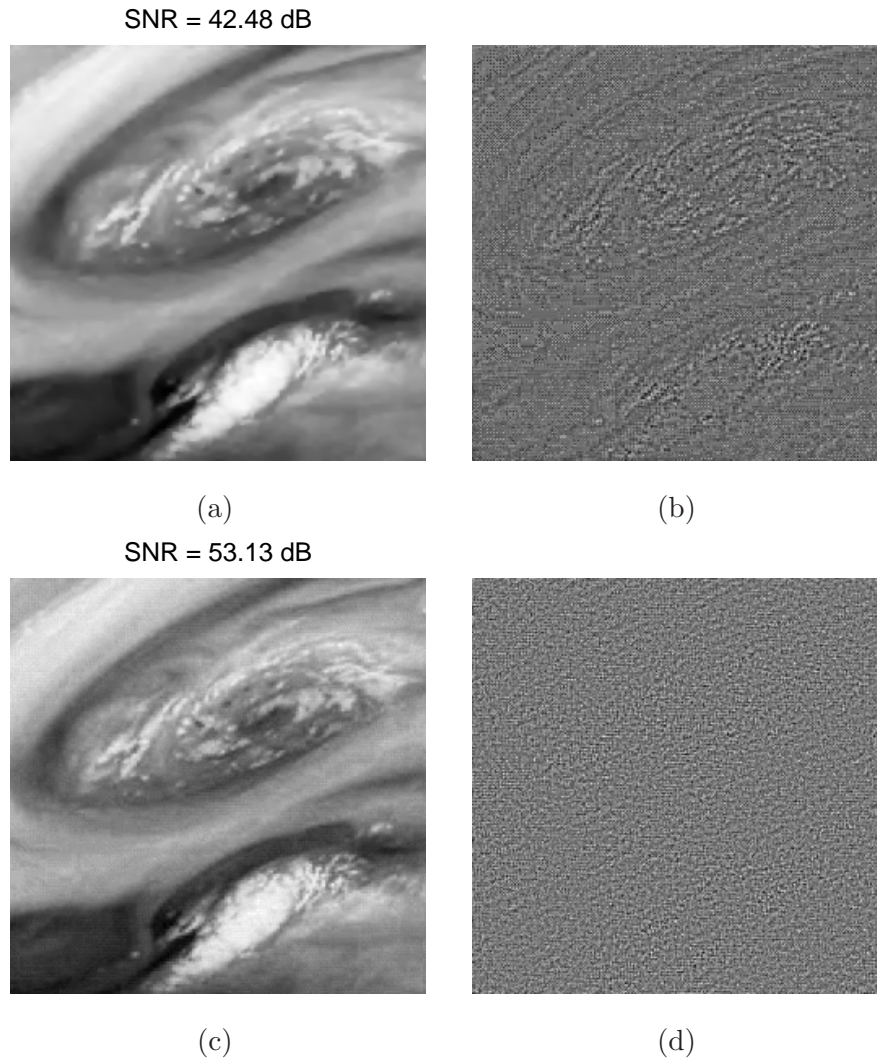

Figure 17: Compressed sensing in remote sensing. (a) Recovery by iterative wavelet thresholding, (b) recovery error by the wavelet method, (c) recovery by iterative curvelet thresholding, (d) recovery error by the curvelet method.

8   FUTURE WORK

The multiresolution geometric analysis technique with curvelets as basis functions is verified as being effective in many fields. However, there are some challenging problems for future work.

1) The computational cost of the curvelet transform is higher than that of wavelets, especially in terms of 3D problems. However, the theory and application of the 3D curvelets are burgeoning areas of research, and it is possible that more efficient curvelet-like transforms will be developed

in the near future. Currently, a fast message passing interface-based parallel implementation can somewhat reduce the cost [77]. How to build a fast orthogonal curvelet transform is still open.

2) How to explore suitable thresholding functions that incorporate and exploit the special characteristics of the curvelet transform? This issue is very important for curvelet applications involving edge detection, denoising, and numerical simulation.

9 ACKNOWLEDGEMENTS

References

[1] F. Andersson, M. de Hoop, H. Smith, G. Uhlmann, A multi-scale approach to hyperbolic evolution equations with limited smoothness, Comm. Partial Differential Equations, **33**, 988-1017 (2008).

[2] I. Bermejo-Moreno, D. Pullin, On the non-local geometry of turbulence, J. Fluid Mech., **603**, 101-135 (2008).

[3] J. Bobin, J. Starck J. Fadili, Y. Moudden, D. Donoho, Morphological component analysis: an adaptative thresholding strategy, IEEE Trans. Image Process., **16** (11), 2675-2681 (2007).

[4] J. Bros, D. Iagolnitzer, Support essentiel et structure analytique des distributions. Séminare Goulaouic-Lions-Schwartz, exp. no. **19** (1975-1976).

[5] E. Candès, Harmonic analysis of neural networks, Appl. Comput. Harmon. Anal., **6**, 197-218 (1999).

[6] E. Candès, L. Demanet, Curvelets and Fourier integral operators, C. R. Math. Acad. Sci. Paris, **336** (5), 395-398 (2003).

[7] E. Candès, L. Demanet, The curvelet representation of wave propagators is optimally sparse, Commun. Pure Appl. Math., **58** (11), 1472-1528 (2005).

[8] E. Candès, L. Demanet, D. Donoho, L. Ying, Fast discrete curvelet transforms, Multiscale Model. Simul., **5** (3), 861-899 (2006).

[9] E. Candès, D. Donoho, Ridgelets: A key to higher-dimensional intermittency?, R. Soc. Lond. Philos. Trans. Ser. A Math. Phys. Eng. Sci., **357**, 2495-2509 (1999).

[10] E. Candès, D. Donoho, Curvelets - a surprisingly effective nonadaptive representation for objects with edges, In Curves and Surface Fitting: Saint-Malo 1999, A. Cohen, C. Rabut, L. Schumaker (Eds.), Vanderbilt Univ. Press, Nashville, 2000, 105-120.

[11] E. Candès, D. Donoho, Continuous curvelet transform: I. Resolution of the wavefront set, Appl. Comput. Harmon. Anal., **19**, 162-197 (2003).

[12] E. Candès, D. Donoho, Continuous curvelet transform: II. Discretization and frames, Appl. Comput. Harmon. Anal., **19**, 198-222 (2003).

[13] E. Candès, D. Donoho, New tight frames of curvelets and optimal representations of objects with piecewise singularities, Comm. Pure Appl. Math., **57**, 219-266 (2004).

[14] E. Candès, F. Guo, New multiscale transforms, minimum total variation synthesis: applications to edge-preserving image reconstruction, Signal Process., **82** (11), 1519-1543 (2002).

[15] E. Candès, J. Romberg, T. Tao, Stable signal recovery from incomplete and inaccurate information, Commun. Pure Appl. Math., **59**, 1207-1233 (2005).

[16] E. Candès, T. Tao, Decoding by linear programming, IEEE Trans. Inform. Theory, **51**, 4203-4215 (2005).

[17] H. Chauris, T. Nguyen, Seismic demigration/migration in the curvelet domain, Geophysics, **73** (2), S35-S46 (2008).

[18] H. Chauris, J. Ma, Seismic imaging in the curvelet domain: achievements and perspectives, 71st EAGE conference and Exhibition, Amsterdam, Netherlands, 8-11 June 2009.

[19] M. Choi, R. Kim, M. Nam, H. Kim, Fusion of multispectral and panchromatic satellite images using the curvelet transform, IEEE Geosci. Remote Sensing Lett., **2** (2), 136-140 (2005).

[20] A. Cordoba, C. Fefferman, Wave packets and Fourier integral operators, Comm. Partial Differential Equations, **3**, 979-1005 (1978).

[21] I. Daubechies, Ten lectures on wavelets, Philadelphia, PA: SIAM, 1992.

[22] L. Demanet, L. Ying, Curvelets and wave atoms for mirror-extend images, Proc. SPIE Wavelets XII, San Diego, August 2007.

[23] L. Demanet, L. Ying, Wave Atoms and Sparsity of Oscillatory Patterns, Appl. Comput. Harmon. Anal., **23** (3), 368-387 (2007).

[24] M. Do, M. Vetterli, The contourlet transform: an efficient directional multiresolution image representation, IEEE Trans. Image Process., **14** (12), 2091-2106 (2005).

[25] D. Donoho, Compressed sensing, IEEE Trans. Inform. Theory, **52** (4), 1289-1306 (2006).

[26] D. Donoho, Wedgelets: nearly minimax estimation of edges, Ann. Statistics, **27** (3), 859-897 (1999).

[27] D. Donoho, X. Huo, Beamlets and multiscale image analysis, in: Multiscale and Multiresolution Methods, Springer Lecture Notes in Comput. Sci. Eng., T. Barth et al. (Eds.), vol. 20, pp. 149-196, 2002.

[28] H. Douma, M. de Hoop, Leading-order seismic imaging using curvelets, Geophysics, **72** (6), S231-S248 (2007).

[29] G. Easley, D. Labate, F. Colonna, Shearlet based total variation for denoising, IEEE Trans. Image Process., **18** (2), 260-268 (2009).

[30] M. Farge, N. Kevlahan, V. Perrier, E. Goirand, Wavelets and turbulence, Proceedings of the IEEE, **84** (4), 639-669 (1996).

[31] M. Farge, G. Pellegrino, K. Schneider, Coherent vortex extraction in 3D turbulent flows using orthogonal wavelets, Phys. Rev. Lett., **87** (5), 45011-45014 (2001).

[32] W. Freeman, E. Adelson, The design and use of steerable filters, IEEE Trans. Pattern Analysis and Machine Intelligence, **13** (9), 891-906 (1991).

[33] X. Gao, T. Nguyen, G. Strang, A study of two-channel complex-valued filter banks and wavelets with orthogonality and symmetry properties, IEEE Trans. Signal Process., **50** (4), 824-833 (2002).

[34] T. Geback, P. Koumoutsakos, Edge detection in microscopy images using curvelets, BMC Bioinformatics, **10** (75),1471-2105-10-75 (2009).

[35] K. Guo, D. Labate, Optimally sparse multidimensional representation using shearlets, SIAM J. Math. Anal., **39**, 298-318 (2007).

[36] G. Hennenfent, F. Herrmann, Seismic denoising with nonuniformly sampled curvelets, Comput. Sci. Eng., **8** (3), 16-25 (2006).

[37] F. Herrmann, G. Hennenfent, Non-parametric seismic data recovery with curvelet frames, Geophysical J. Int., **173** (1), 233-248 (2008).

[38] F. Herrmann, P. Moghaddam, C. Stolk, Sparsity- and continuity-promoting seismic image recovery with curvelet frames, Appl. Comput. Harmon. Anal., **24** (2), 150-173 (2008).

[39] F. Herrmann, D. Wang, D. Verschuur, Adaptive curvelet-domain primary-multiple separation, Geophysics, **73** (3), A17-A21 (2008).

[40] L. Jiang, X. Feng, H. Yin, Structure and texture image inpainting using sparse representations and an iterative curvelet thresholding approach, Int. J. Wavelets, Multiresolution and Inform. Process., **6** (5), 691-705 (2008).

[41] N. Kingsbury, Image processing with complex wavelets, Phil. Trans. R. Soc. Lond. A, **357**, 2543-2560 (1999).

[42] N. Kingsbury, Complex wavelets for shift invariant analysis and filtering of signals, Appl. Comput. Harmon. Anal., **10** (3), 234-253 (2001).

[43] D. Labate, W-Q. Lim, G. Kutyniok, and G. Weiss. Sparse multidimensional representation using shearlets, SPIE Proc. Wavelets XI, vol. 5914, pp. 254-262, San Diego, CA, 2005.

[44] T. Lee, Image representation using 2D Gabor wavelets, IEEE Trans. Pattern Analysis and Machine Intelligence, **18** (10), 1-13 (2008).

[45] T. Lin, F. Herrmann, Compressed extrapolation, Geophysics, **72** (5), SM77-SM93 (2007).

[46] Y. Lu, M. N. Do, Multidimensional directional filter banks and surfacelets, IEEE Trans. Image Process., **16** (4), 918-931 (2007).

[47] J. Ma, Curvelets for surface characterization, Appl. Phys. Lett., **90**, 054109 (2007).

[48] J. Ma, Deblurring using singular integrals and curvelet shrinkage, Physics Letters A, **368**, 245-250 (2007).

[49] J. Ma, Single-pixel remote sensing, IEEE Geosci. Remote Sensing Lett., **6** (2), 199-203 (2009).

[50] J. Ma, A. Antoniadis, F.-X. Le Dimet, Curvelet-based multiscale detection and tracking for geophysical fluids, IEEE Trans. Geosci. Remote Sensing, **44** (12), 3626-3637 (2006).

[51] J. Ma, F.-X. Le Dimet, Deblurring from highly incomplete measurements for remote sensing, IEEE Trans. Geosci. Remote Sensing, **47** (3), 792-802 (2009).

[52] J. Ma, M. Fenn, Combined complex ridgelet shrinkage and total variation minimization, SIAM J. Sci. Comput., **28** (3), 984-1000 (2006).

[53] J. Ma, M. Hussaini, Three-dimensional curvelets for coherent vortex analysis of turbulence, Appl. Phys. Lett., **91**, 184101 (2007).

[54] J. Ma, M. Hussaini, O. Vasilyev, F.-X. Le Dimet, Multiscale geometric analysis of turbulence by curvelets, Physics of Fluids, **21**, 075104 (2009).

[55] J. Ma, G. Plonka, Combined curvelet shrinkage and nonlinear anisotropic diffusion, IEEE Trans. Image Process., **16** (9), 2198-2206 (2007).

[56] J. Ma, G. Tang, M. Y. Hussaini, A refining estimation for adaptive solution of wave equation based on curvelets, in Wavelets XII, D. Van De Ville, V. K. Goyal, M. Papadakis (Eds.), Proc. of SPIE, Vol. 6701, pp. 67012J, San Diego, CA, 2007.

[57] S. Mallat, Wavelets for a vision, Proceedings of The IEEE, **84** (4), 604-614 (1996).

[58] S. Mallat, G. Peyré, A review of bandlet methods for geometrical image representation, Numer. Algorithms, **44** (3), 205-234 (2007).

[59] R. Neelamani, A. Baumstein, D. Gillard, M. Hadidi, W. Soroka, Coherent and random noise attenuation using the curvelet transform, the leading edge, **27** (2), 240-248 (2008).

[60] J. Neumann, G. Steidl, Dual–tree complex wavelet transform in the frequency domain and an application to signal classification, Int. J. Wavelets, Multiresolution and Inform. Process., **3** (1), 43-66 (2005).

[61] E. Le Pennec, S. Mallat, Sparse geometrical image approximation with bandlets, IEEE Trans. Image Process., **14** (4), 423-438 (2005).

[62] B. Olshausen, D. Field, Emergence of simple-cell receptive filed properties by learning a sparse code for natural images, Nature, **381**, 607-609 (1996).

[63] B. Olshausen, D. Field, Sparse coding of sensory inputs, Current Opinion in Neurobiology, **14**, 481-487 (2004).

[64] G. Plonka, J. Ma, Nonlinear regularized reaction-diffusion filters for denoising of images with textures, IEEE Trans. Image Process., **17** (8), 1283-1294 (2008).

[65] G. Plonka, J. Ma, Curvelet-wavelet regularized split Bregman method for compressed sensing, preprint, 2009.

[66] H. Shan, J. Ma, H. Yang, Comparisons of wavelets, contourlets, and curvelets for seismic denoising, J. Applied Geophysics, 2009, to appear.

[67] E. Simoncelli, W. Freeman, E. Adelson, D. Heeger, Shiftable multiscale transforms, IEEE Trans. Inform. Theory, **38** (2), 587-607 (1992).

[68] H. F. Smith, A Hardy space for Fourier integral operators, J. Geom. Anal., **8**, 629-653 (1998).

[69] J. Starck, E. Candès, D. Donoho, The curvelet transform for image denoising, IEEE Trans. Image Process., **11**, 670-684 (2002).

[70] J. Starck, E. Candès, D. Donoho, Astronomical image representation by the curvelet transform, Astronomy and Astrophysics, **398**, 785-800 (2003).

[71] J. Starck, F. Murtagh, E. Candès, F. Murtagh, D. Donoho, Gray and color image contrast enhancement by the curvelet transform, IEEE Trans. Image Process., **12** (6), 706-717 (2003).

[72] J. Starck, M. Elad, D. Donoho, Image decomposition via the combination of sparse representation and a variational approach, IEEE Trans. Image Process., **14** (10), 1570-1582 (2005).

[73] B. Sun, J. Ma, H. Chauris, H. Yang, Solving the wave equation in the curvelet domain: a mulitscale and multidirectional approach, J. Seismic Exploration, 2009, to appear.

[74] W. Tan, J. Ma, F. Herrmann, Improved compressed sensing for curvelet-based seismic data reconstruction, Preprint, 2009.

[75] L. Tessens, A. Pizurica, A. Alecu, A. Munteanu, W. Philips, Context adaptive image denoising through modeling of curvelet domain statistics, J. Electronic Imaging, **17** (3), 03021:1-17 (2008).

[76] R. Willett, K. Nowak, Platelets: A multiscale approach for recovering edges and surfaces in photon-limited medical imaging, IEEE Trans. Med. Imaging, **22** (3), 332-350 (2003).

[77] L. Ying, L. Demanet, E. Candès, 3D Discrete Curvelet Transform, Proc. of SPIE Wavelets XI, Vol. 5914, pp. 591413, San Diego, CA, 2005.

[78] B. Zhang, J. Fadili, J. Starck, Wavelets, ridgelets, and curvelets for Poisson noise removal, IEEE Trans. Image Process., **17** (7), 1093-1108 (2008).

[79] C. Zhang, L. Cheng, Z. Qiu, L. Cheng, Multipurpose watermarking based on multiscale curvelet transform, IEEE Trans. Inform. Forensics and Security, **3** (4), 611-619 (2008).

Jianwei Ma received the Ph.D. degree in solid mechanics from Tsinghua University in 2002. He has been a Visiting Scholar, Postdoctoral Research Fellow, and Guest Professor with the University of Cambridge, University of Oxford, University of Huddersfield, University of Grenoble (INRIA), and University of Duisburg-Essen. Since 2006, he has been an Assistant Professor with the School of Aerospace, and a Research Director with the Institute of Seismic Exploration, Tsinghua University. From June to August 2006, he was a Visiting Professor in Swiss Federal Institute of Technology (EPFL). From June to September 2007, he was a Visiting Professor in Florida State University and University of Colorado at Boulder. In May 2008 and from March to September 2009, he was an Invited Professor in INRIA-Grenoble and Ecole des Mines de Paris. His research interests include wavelets, curvelets, image processing, compressed sensing, remote sensing and seismic exploration. He is an Editor of Int. J. Artificial Intelligence. Contact him at jma@tsinghua.edu.cn.

Gerlind Plonka received the Diploma degree in mathematics from the University of Rostock (Germany), in 1990, and the Ph.D. degree in mathematics as well as the Habilitation from the University of Rostock, in 1993 and 1996, respectively. Since 1998, she is Associate Professor for Applied Analysis at the University of Duisburg-Essen. Her current research interests include wavelet and frame theory, Fourier analysis, nonlinear diffusion and applications in signal and image processing. Contact her at gerlind.plonka@uni-due.de.